JGR Space Physics

RESEARCH ARTICLE
10.1029/2021JA029947

Primary Versus Secondary Gravity Wave Responses at F-Region Heights Generated by a Convective Source

C. J. Heale[1], P. A. Inchin[1], and J. B. Snively[1]

[1]Center for Space and Atmospheric Research (CSAR) and Physical Sciences Department, Embry-Riddle Aeronautical University, Daytona Beach, FL, USA

Key Points:

- Numerical simulations are performed to understand the dynamics of primary and secondary GWs from a thunderstorm-like line source
- The sound speed minimum near mesopause does not provide a decisive upper limit on GW phase speeds for separating primary versus secondary waves
- Primary waves with fast phase speeds may tunnel through intervening layers of evanescence as they propagate from the source to thermosphere

Supporting Information:

Supporting Information may be found in the online version of this article.

Correspondence to:

C. J. Heale,
healec@my.erau.edu

Citation:

Heale, C. J., Inchin, P. A., & Snively, J. B. (2022). Primary versus secondary gravity wave responses at F-region heights generated by a convective source. *Journal of Geophysical Research: Space Physics*, *127*, e2021JA029947. https://doi.org/10.1029/2021JA029947

Received 7 SEP 2021
Accepted 13 DEC 2021

Abstract A 2D nonlinear, compressible model is used to simulate the acoustic-gravity wave (AGW, i.e., encompassing the spectrum of acoustic and gravity waves) response to a thunderstorm squall-line type source. We investigate the primary and secondary neutral AGW response in the thermosphere, consistent with waves that can couple to the F-region ionospheric plasma, and manifest as Traveling Ionospheric Disturbances (TIDs). We find that primary waves at $z = 240$ km altitude have wavelengths and phase speeds in the range 170–270 km, and 180–320 m/s, respectively. The secondary waves generated have wavelengths ranging from ∼100 to 600 km, and phase speeds from 300 to 630 m/s. While there is overlap in the wave spectra, we find that the secondary waves (i.e., those that have been nonlinearly transformed or generated secondarily/subsequently from the primary wave) generally have faster phases than the primary waves. We also assess the notion that waves with fast phase speeds (that exceed proposed theoretical upper limits on passing from the mesosphere to thermosphere) observed at F-region heights must be secondary waves, for example, those generated in situ by wave breaking in the lower thermosphere, rather than directly propagating primary waves from their sources. We find that primary waves with phase speeds greater than this proposed upper limit can tunnel through a deep portion of the lower/middle atmosphere and emerge as propagating waves in the thermosphere. Therefore, comparing a TID's/GWs phase speed with this upper limit is not a robust method of identifying whether an observed TID originates from a primary versus secondary AGW.

1. Introduction

Traveling ionospheric disturbances (TIDs) are transient, propagating plasma perturbations in the ionosphere that have been historically characterized into small- (SSTID), medium- (MSTID), and large-scale (LSTID) (Hocke & Schlegel, 1996; Hunsucker, 1982) motions. Across all scales, TIDs range from hundreds to thousands of kilometer with phase speeds of a few hundred meters per second (Hunsucker, 1982; M. C. Kelley, 2011). TIDs have been observed for many decades using instruments such as HF Doppler radars (Oinats et al., 2016; Waldock & Jones, 1986), ionosondes (Amorim et al., 2011; MacDougall et al., 2011; Munro, 1948), GPS/GNSS-derived Total Electron Content (TEC) (Azeem & Barlage, 2018; Azeem et al., 2017, 2015; Chen et al., 2019; Chou et al., 2017; Figueiredo et al., 2018; Nishioka et al., 2013; Otsuka et al., 2013; Saito et al., 1998; Xu et al., 2019), airglow imagers (Heale et al., 2019; Huang et al., 2016; Martinis et al., 2010; Paulino et al., 2016; Pimenta et al., 2008; Shiokawa et al., 2003; Takahashi et al., 2020), and satellite beacons (Forbes et al., 2016; R. F. Garcia et al., 2016; Park et al., 2015).

One significant source of MSTIDs is the direct driving by acoustic-gravity waves (AGWs) (Hocke & Schlegel, 1996; Hunsucker, 1982; Kirchengast, 1996; Nicolls et al., 2014; Otsuka, 2018; Zettergren & Snively, 2015) which can produce TEC amplitude oscillations of 0.1–1 TEC unit (1 TECu = 1×10^{16} electrons/m^2 column) (Takahashi et al., 2020). AGWs are propagating waves in the neutral atmosphere, including compressional acoustic waves and buoyant gravity waves, that are generated from a variety of lower atmospheric sources such as deep convection, flow over topography, natural hazards, and adjustment processes (Fritts & Alexander, 2003; Hines, 1960). AGWs grow in amplitude as they propagate upward into the atmosphere due to the decreasing background atmospheric mass density, and carry energy and momentum along with them. Approximately, saturation occurs for these AGWs when their amplitude approaches their phase speed (if not subject to instability prior, due to interactions with the ambient state), and the waves will break, depositing their energy and momentum into the mean flow (Fritts & Alexander, 2003; Holton, 1983; Holton & Alexander, 2000; Lindzen, 1981; Lund & Fritts, 2012; McFarlane, 1987). AGWs with large phase speeds and vertical wavelengths can avoid breaking in the middle atmosphere and propagate into the thermosphere/ionosphere, where they undergo linear viscous

damping and/or nonlinear breaking (when at larger amplitude) (Heale et al., 2014; Hickey et al., 2009; Pitteway & Hines, 1963; Vadas, 2007; Vadas & Fritts, 2005; Vadas & Liu, 2009), which also transfer energy and momentum into the ambient atmosphere.

An AGW propagating through the thermosphere manifests itself as an MSTID through collisions between neutral particles and ionospheric plasma. While the neutral perturbations induced by AGWs are constrained primarily by the waves' polarization relations, ions are also confined to anisotropic motions along the Earth's magnetic field lines. As such, AGW MSTIDs are not direct tracers of the AGW but do rely on their presence to be sustained (Klostermeyer, 1972; Yeh & Liu, 1974; Kirchengast, 1996; Hocke & Schlegel, 1996; Vadas & Crowley, 2017). While it is suggested that daytime MSTIDs are manifestations of AGWs (Figueiredo et al., 2018; Hines, 1960; Hooke, 1968; Hunsucker, 1982; Kirchengast, 1996; Kotake et al., 2007; Otsuka et al., 2013; Tsugawa et al., 2007; Xiao et al., 2007), some nighttime mid-latitude MSTIDs have a specific alignment and propagation direction that cannot be explained by AGW theory. These MSTIDs propagate NW–SE in the northern hemisphere, and NE–SW in the southern hemisphere (Behnke, 1979; Hernández-Pajares et al., 2012; Kotake et al., 2006; Rajesh et al., 2016; Saito et al., 1998; Tsugawa et al., 2007). They are suggested to be generated by electrodynamic coupling of the Perkins instability (Perkins, 1973; M. C. Kelley & Makela, 2001; Shiokawa et al., 2003; Cosgrove et al., 2004; Makela et al., 2010; Huang et al., 2016; Narayanan et al., 2018), however, the instability growth rate is too small to account for the observations (M. C. Kelley & Makela, 2001; F. J. Garcia et al., 2000). Therefore, studies have suggested that AGW forcing assists in enhancing the Perkins instability to generate these specifically aligned nighttime MSTIDS (M. C. Kelley & Fukao, 1991; M. Kelley & Miller, 1997; M. C. Kelley & Makela, 2001; Shiokawa et al., 2003; Makela et al., 2010; Yokoyama et al., 2009; Cosgrove & Tsunoda, 2004; Tsunoda, 2010; Krall et al., 2013; Chou et al., 2017). Therefore, AGWs are intrinsically linked to discussions on the origin of MSTIDs.

AGWs and their manifestation as MSTIDs have been observed and studies using multilayer observations from ground and satellite instrumentation (Azeem & Barlage, 2018; Azeem et al., 2017, 2015; Chou et al., 2017; Crowley et al., 2016; Figueiredo et al., 2018; Heale et al., 2019; Nishioka et al., 2013; Takahashi et al., 2020; Xu et al., 2019). These MSTIDs typically have periods from 10 to 50 min, horizontal wavelengths of 100–400 km, and phase speeds from 100 to 500 m/s (Azeem & Barlage, 2018; Azeem et al., 2017, 2015; Chou et al., 2017; Vadas & Azeem, 2021; Xu et al., 2019). However, linking the MSTIDs seen in the ionosphere to AGWs in the neutral atmosphere and their sources can be difficult, even with multilayer observation, for a number of reasons. First, AGW sources can be complex and the exact spectra of AGWs generated by those sources are not well constrained due to the wide range of scales and amplitudes. Second, as AGWs propagate through the atmosphere they are subject to refraction, reflection, ducting, and filtering by the background atmospheric winds and temperature structure which changes the wave spectra with altitude. Third, dissipation mechanisms lead to selective filtering of wave modes between the source and the ionosphere. Finally, observational techniques are often biased toward certain wave modes due to viewing angles, temporal and spatial resolution, observation period, layer depths, integrated layer of observations, etc. To complicate matters further, waves that dissipate and/or break can generate subsequent waves that continue to propagate upwards (Vadas et al., 2018; Zhou et al., 2002; Chun & Kim, 2008; Heale, Bossert, et al., 2020; Bossert et al., 2017). Breaking and wave dissipation, leading to subsequent wave responses, are known to be prominent in the mesosphere and lower thermosphere (Heale, Bossert, et al., 2020; Heale, Lund, & Fritts, 2020; Chun & Kim, 2008; Horinouchi et al., 2002; Vincent et al., 2013; J. Snively & Pasko, 2003; R. Walterscheid et al., 2001; Vadas et al., 2003; Vadas & Becker, 2019; Lund & Fritts, 2012; Bossert et al., 2017). Thus, it is difficult to ascertain whether MSTIDs in the ionosphere are primary waves generated by a lower atmospheric source, or waves transformed or generated subsequently by wave breaking/dissipation processes.

Studies have suggested that some of the MSTIDs observed above convective sources are secondary waves generated from primary wave breaking and dissipation in the mesosphere/lower thermosphere (Azeem & Barlage, 2018; Miyoshi et al., 2018; Vadas & Azeem, 2021; Vadas & Crowley, 2010), and these secondary wave driven MSTIDs can be identified by their phase speeds (Vadas & Azeem, 2021; Vadas & Crowley, 2010). Their rationale is that the observed phase speeds of the MSTIDs are faster than theoretical upper limits for GW propagation at mesopause (~280 m/s) (Vadas & Azeem, 2021; Vadas & Crowley, 2010; Vadas et al., 2019). This "bottleneck" region for AGWs results from a minima in the speed of sound near the mesopause and the upper limit for AGW phase speeds that can pass through this "bottleneck" is ~98% of the local sound speed (Vadas et al., 2019). Therefore,

AGWs generated by a convective source in the troposphere, with phase speeds greater than this limit, should not be able to pass the mesopause into the thermosphere. Thus, Vadas and Crowley (2010) suggested that any waves in the ionosphere with phase speeds above this limit must be secondary waves (we use secondary as a generic term to refer to all wave generation subsequent to the primary wave) generated in the thermosphere. Vadas and Crowley (2010) and Vadas and Azeem (2021) derived this result from linear theory and implemented reverse ray-tracing to show that MSTIDs could not exist below the mesopause. However, these investigations do not account for effects such as wave tunneling which may influence the validity of these conclusions (e.g., Sutherland & Yewchuk, 2004, and references within) which may influence the validity of these conclusions especially for the spectrum of acoustic-gravity waves for which coupling through evanescence may occur over deep ranges of altitude (R. L. Walterscheid & Hecht, 2003). Vadas and Crowley (2010) and Vadas and Azeem (2021) also noted that the primary wave spectra and the secondary wave spectra generated by the storm studied were very similar and overlap particularly in the 100–200 m/s phase speed range.

Wave tunneling is a process in which a wave moves from a region in which it is able to propagate, through a region in which it is evanescent (i.e., where it cannot exist as a propagating wave), to emerge as a propagating wave in a third region. Regions of evanescence exist where the buoyancy frequency of the atmosphere is greater than the intrinsic frequency of a given wave, thus, it does not support buoyant motions when perturbed over those timescales. Regions of evanescence for waves that are able to propagate at other altitudes can occur via changes in the temperature of the atmosphere with altitude (which changes the atmosphere's stability and thus the buoyancy frequency) or by changes in the wind with altitude (which changes the wave's intrinsic frequency). The altitude at which the buoyancy frequency matches the intrinsic frequency of the wave is known as a turning point, or reflection level. At this point, the vertical wavenumber of the wave approaches 0 (vertical wavelength of the wave approaches infinity) and the wave begins to reflect vertically. However, the wave solution in the evanescent region above the reflection point is not zero but an exponentially decaying one (e^{-mz}). If the depth of the layer of evanescence is small relative to the vertical decay scales of the wave, which is more likely for waves that exhibit relatively high phase velocities, then some of the energy associated with the wave can survive this exponentially decay and resume propagation where the atmosphere supports buoyant motions again.

In this paper, we use a 2D nonlinear and compressible simulation of an idealized thunderstorm to assess the origin of fast phase speed (greater than the "bottleneck" upper limit) GWs observed at ionospheric altitudes. We find that primary waves with phase speeds greater than the theoretical "bottleneck" limit can indeed propagate to ionospheric heights through tunneling mechanisms and need not be waves generated subsequently in the thermosphere. That is not to say that all fast phase speed waves observed as TIDs are primary waves, but it cannot be ruled out that they are not as is suggested in Vadas and Crowley (2010) and Vadas and Azeem (2021). The paper is laid out as follows: Section 2 describes the numerical model, source, and ambient atmosphere. Section 3 demonstrates the theoretical upper limits on gravity wave phase speeds. Section 4 presents the simulation results and analysis of the wave spectra of GWs in the neutral atmosphere at lower part of ionospheric F-region heights, and their origin. Section 5 serves as summary and conclusions.

2. Numerical Models and Setup

Gravity wave generation and propagation through the neutral atmosphere is simulated using the time-dependent, high-resolution numerical Model for Acoustic-Gravity wave Interactions and Coupling (MAGIC) (J. B. Snively & Pasko, 2008; J. B. Snively, 2013; Zettergren & Snively, 2015). MAGIC solves the nonlinear, fully compressible Euler equations in conservation law form and includes gravity as a balanced source term, solving time-split coupled equations for the Navier-Stokes viscosity (allowing for wave dissipation due to molecular viscosity and thermal conduction) (J. B. Snively & Pasko, 2008; J. B. Snively, 2013). MAGIC uses a finite volume approach (LeVeque, 2002; LeVeque & Berger, 2004) which decomposes flux differences between cell boundaries into characteristic "f-waves" (Bale et al., 2002), each of which propagate at characteristic speeds. Additional details and the full equations can be found in Appendix A1 of Zettergren and Snively (2015).

2.1. Wave Forcing and Simulation Domain

Gravity waves are excited in MAGIC via a spatially and temporally varying latent heat source that represents thunderstorm cells. The latent heating profile is derived from the Stephan and Alexander (2015) algorithm with

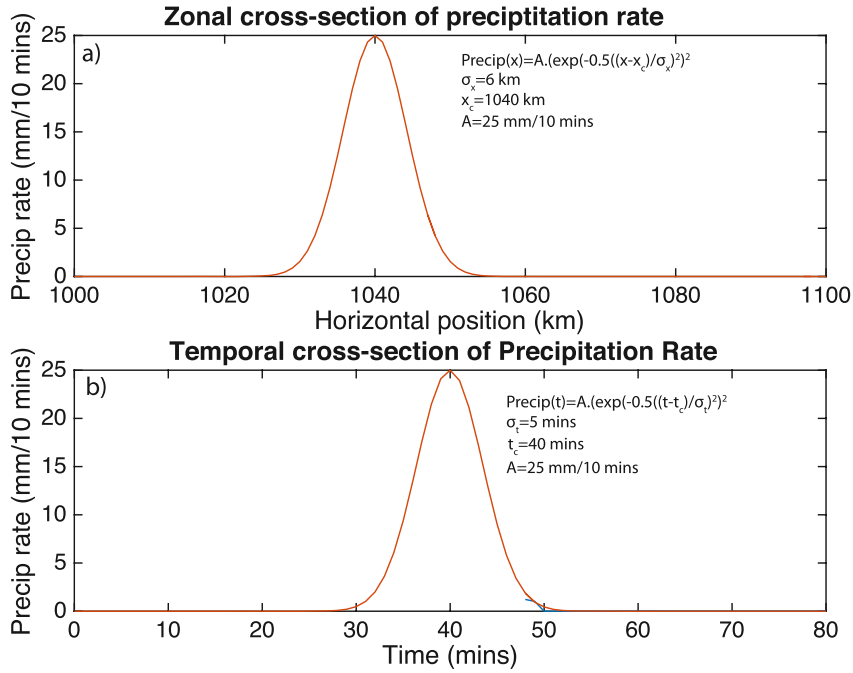

Figure 1. Gaussian representation of (a) the thunderstorm precipitation rate in x (zonal), and (b) in time which is input into the Stephan and Alexander (2015) algorithm to generate the model latent heating.

Doppler radar precipitation rates from the Next Generation Radar (NEXRAD) network as input. The Stephan and Alexander (2015) algorithm was created by fitting a linear regression to latent heating profile parameters (dependent variables) with precipitation rates (mm/10 min) as the independent variable. The relations were derived from the full-physics weather research and forecasting (WRF) model and validated against atmospheric infrared sounder (AIRS) observations.

For simplification of the analysis and to reduce the computational expense, the simulation is run in 2D (zonal-altitude). The storm cell used for this simulation has a half width of 6 km in zonal extent (km) and 5 min in time with a maximum precipitation rate of 25 mm/10 min. While the 25 mm/10 min peak precipitation rate is greater than the range of precipitation rates tested in the Stephan and Alexander (2015) algorithm, this is not atypical of strong thunderstorms which produce tropopause overshoot associated with gravity wave generation. The spatial and temporal widths are chosen to be typical of convective cells which, on average, have a diameter of ∼10 km and a lifetime of 20–30 min (Stull, 2017). As this is a 2D simulation, the convective cell effectively represent a line source in the meridional direction (similar to a squall line). We note that this assumption will lead to a more coherent, planar wave response with larger amplitudes, and stronger wave-mean flow interactions, than in a full 3D simulation where geometric dispersion can occur. Wave breaking will also not evolve as it would in 3D. Dong et al. (2020) and Fritts et al. (2020) noted that GW packets in 3D versus 2D are less efficient sources of secondary waves while the decay of instabilities is more efficient when 3D breaking is permitted. Typically, as eddies resulting from breaking reach maximum altitude, three dimensional motions occur which initiate the turbulent collapse of these eddies (Scinocca & Ford, 2000). Thus, we have also run simulations at 1/4 and 1/100 of the original amplitude for comparison and to assess the effects of nonlinearity with increasing source amplitude. These results will be discussed later. The Gaussian squared precipitation rate is an input into the Stephan and Alexander (2015) algorithm to produce the latent heating within MAGIC model. The full analytical expression for the precipitation rate is given below which is displayed graphically in Figure 1.

$$Precip(x,t) = A \cdot \exp\left[-\frac{(x-x_c)^2}{2\sigma_x^2} - \frac{(t-t_c)^2}{2\sigma_t^2}\right]^2 \quad (1)$$

where $A = 25$ mm/10 min, $x_c = 1040$ km, $\sigma_x = 6$ km, $t_c = 40$ min, and $\sigma_t = 5$ min.

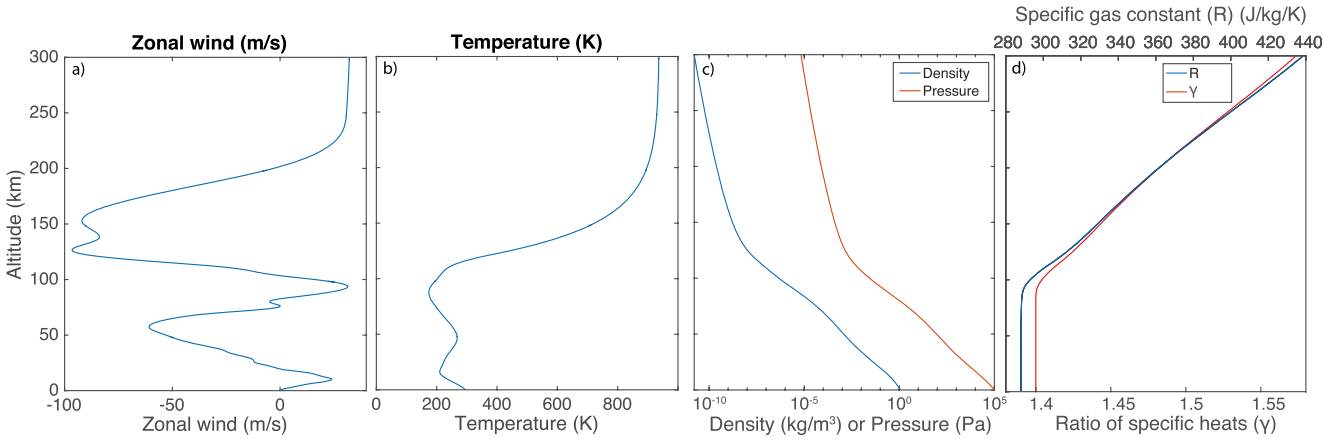

Figure 2. The (a) zonal wind, (b) temperature, (c) density pressure, and (d) ratio of specific heats and specific gas constant profiles used as ambient atmospheric states for the simulation.

The numerical domain is chosen as 2,400 km in zonal (x) direction and 500 km in altitude, with 1 km uniform resolution. Model outputs sampling rate is 60 s with the simulation running for 160 min. A sponge layer is applied to the top 30 km of the domain. The bottom boundary is closed (reflective), while the side and upper boundaries are open.

2.2. Background Atmospheric State

The background ambient density and temperature structure for the simulation are taken from the NRLMSISE-00 model (Picone et al., 2002) and the zonal winds are specified using MERRA-2 between 0 and 60 km altitude and the HWM07 model (Drob et al., 2008) from 60 to 500 km altitude. The background ambient state is a fixed vertical profile defined at a latitude of 37.5°N, a longitude of 93°W, and at 6 UT on 8 July 2016. This position and time is chosen to coincide with the location of the storm cell. The temperature, wind, density, pressure, ratio of specific heats, and specific gas constant profiles are shown in Figure 2.

2.3. Phase Speed Limitations Imposed by the Ambient Atmosphere

The ambient wind and temperature structure imposes theoretical limits on the phase speeds of both acoustic and gravity waves that can freely propagate through the atmosphere. The minimum phase speeds for gravity waves are defined by the wind speed itself (U); waves with phase velocities smaller than the local wind velocity (along the direction of wave propagation) will be subject to refraction to small scales leading to "critical level" filtering. The speed of sound as defined by:

$$C_s = \sqrt{\gamma RT} \tag{2}$$

where γ is the ratio of specific heats, R is the ideal gas constant and T is the temperature which varies with altitude. While the speed of sound defines the phase speed for acoustic waves, Vadas et al. (2019) derived an expression for the maximum intrinsic phase speed ($C_p - U$) at which an internal gravity wave can propagate in relation to the speed of sound given by:

$$\max(C_{pI}) = \frac{2\sqrt{\gamma - 1}}{\gamma} \cdot C_s \tag{3}$$

However, this expression is derived assuming an isothermal atmosphere. A more general expression for the upper limit on the gravity wave phase speed allowing for a varying ambient temperature is:

$$\max(C_{pI}) \sim 2NH \tag{4}$$

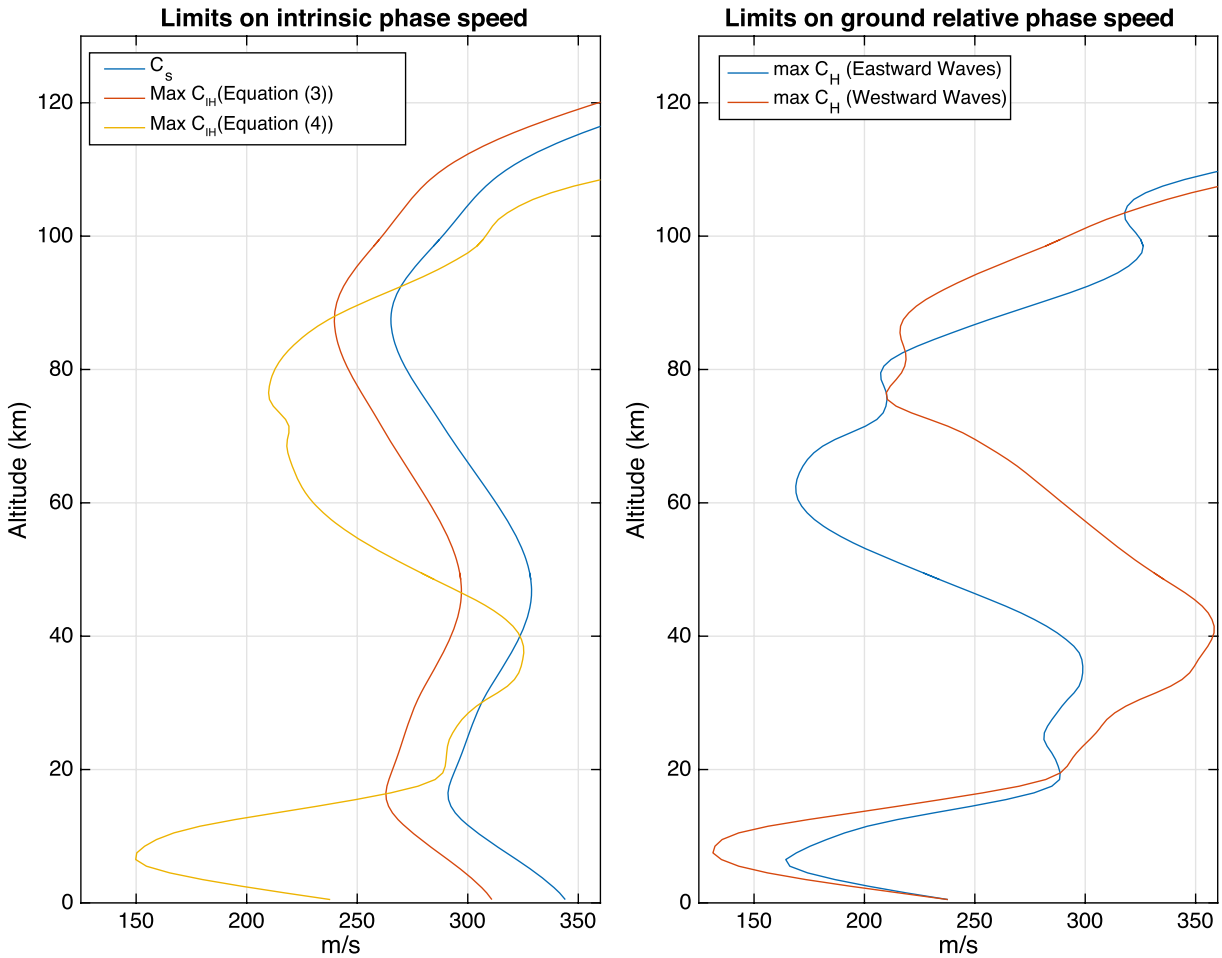

Figure 3. The (a) speed of sound, and theoretical maximum intrinsic phase speeds (under isothermal and nonisothermal conditions) and (b) the theoretical maximum ground relative phase speeds for eastward and westward propagating waves.

where N is the buoyancy frequency of the atmosphere and H is the density scale height (RT/g) (Vadas & Crowley, 2010). This expression represents the phase speed at which the vertical and horizontal wavelength's tend to infinity and also the limit at which a wave is reflected (turning point level). Since both of the above definitions impose maximum intrinsic phase speed, the equivalent maximum ground relative phase speed is thus given by:

$$\max(C_p) = \max(C_{pI}) + U \tag{5}$$

where U is the wind along the direction of wave propagation (note this term is negative if the wind and wave are opposing each other). This shows that the wind, and its direction relative to the wave propagation direction, can have significant influences on the theoretical internal wave phase speeds. Linear theory suggests that a purely monochromatic wave will be completely reflected at the turning point level and will be evanescent (subject to an exponentially decaying amplitude) above this level. However, this does not take into account that GWs may also tunnel through an evanescent region of finite depth and emerge from the layer as a propagating waves again (Jones, 1970; Fritts & Yuan, 1989; R. L. Walterscheid & Hecht, 2003; Sutherland & Yewchuk., 2004).

Figure 3a shows the speed of sound and theoretical maximum intrinsic phase speeds as a function of altitude as described by Equations 2–4. A minimum in the speed of sound occurs at the mesopause (87 km) with a value of 265 m/s Equation 3 then suggests a minimum in the imposed maximum intrinsic gravity wave phase speed at the same height but with a value of 239 m/s. This region is described as the "bottleneck" altitude for waves (Vadas & Azeem, 2021; Vadas & Crowley, 2010; Vadas et al., 2019) as it is proposed to act as a barrier confining waves with phase speeds greater than the bottleneck maximum speed (239 m/s in this case) to the lower atmosphere and allowing waves with smaller phase speeds to pass from the lower/middle atmosphere into the thermosphere. For

this reason, it is later cited that waves observed in the thermosphere/ionosphere with intrinsic phase speeds greater than this bottleneck speed, could not have originated from a tropospheric source and must have been generated in the thermosphere as a secondary wave (Vadas & Azeem, 2021). However, the expression in Equation 3 only applies for an isothermal atmosphere which, when considering propagation between the Earth's surface and the thermosphere, is not a realistic assumption. Using the more general expression for the maximum gravity wave phase speed, which does not have the isothermal restriction (Equation 4), leads to a mesospheric minimum in the maximum allowable phase speed at 78 km altitude with an intrinsic phase speed of 210 m/s. There is a stark difference in the shape of the profile between the limits defined by Equations 3 and 4. In particular, there are far more restrictive conditions in the troposphere using Equation 4 with a minimum at 6.5 km with a maximum allowable intrinsic phase speed of 150 m/s. However, the definition using Equation 4 also suggests a maximum allowable intrinsic phase speed that is greater than the speed of sound between 30 and 40 km altitude, which appears less restrictive. Therefore, both interpretations have caveats, and neither address the potential role for tunneling in upward propagation.

For a rigorous examination of the restrictions, the full dispersion relationship should be used with a known wave period and wavelength. And, to assess upward wave propagation, a full-wave numerical solution accounting rigorously for reflection, evanescence, and tunneling is needed.

Since model simulations show GW propagation relative to the ground, Figure 3b shows the maximum allowable ground relative phase speed (Equation 5), with the maximum intrinsic phase speed imposed by Equation 4, for eastward and westward propagating waves respectively. For eastward propagating waves, Figure 3b shows mesospheric minima occurs at an altitude of 62 km with a phase speed of 170 m/s. For westward propagating waves, a mesospheric minimum exists at 75.5 km altitude at a phase speed of 210 m/s. Therefore, we would not expect to see primary waves in the thermosphere that exceed 170 m/s which are propagating eastward or 210 m/s which are propagating westward. However, the atmosphere supports much faster westward waves in the stratosphere (up to 360 m/s at 40 km) compared to eastward but much smaller phase speeds in the troposphere. The assumption is that waves generated by convection predominantly occur from tropopause overshoot where the limit on phase speeds is much larger than in the lower troposphere. In the thermosphere (at $z = 240$ km), the speed of sound increases to 735 m/s and can support much faster waves than the lower atmosphere. The validity of these theoretical limits in practice, where evanescence may still enable tunneling, will be tested against the simulation results in the following sections.

3. Simulation Results

This section splits the analysis of the simulation results into a time frame when only primary waves are present, and another—when both primary and secondary waves are present. The MAGIC simulation results are presented in terms of neutral temperature perturbation (K). Please see the Supporting Information S1 for movies of the simulation results.

3.1. Primary Wave Response

3.1.1. Primary Wave Evolution

Figure 4 shows the GW-induced temperature perturbation at $t = 50$–70 min. Beyond $t = 80$ min, breaking occurs and secondary waves are generated. Therefore, by limiting the analysis in this section to times before $t = 80$ min, we can better assess the primary wave spectra and characteristics generated by the convective source. Figure 4 clearly shows the generation of acoustic, acoustic-gravity (AGW), and gravity waves that propagate, from the source, up into the thermosphere and reach ionospheric heights. All the waves seen in Figure 4 are primary waves and the eastward waves have clear continuous phases that can be traced back to the tropospheric source. The phases of the westward waves do not, at first glance, appear to connect all the way back to the source region and there appears to be two distinct regions of propagation. The first region of propagation occurs between 10 and 50 km altitude and a second above ∼105 km altitude. We note that there is a local maxima in the westward wind at 50 km altitude which will lead to critical level filtering of the westward waves. The scales of the waves vary dramatically with altitude and are subject to refraction by the vertically varying zonal wind and ambient temperature.

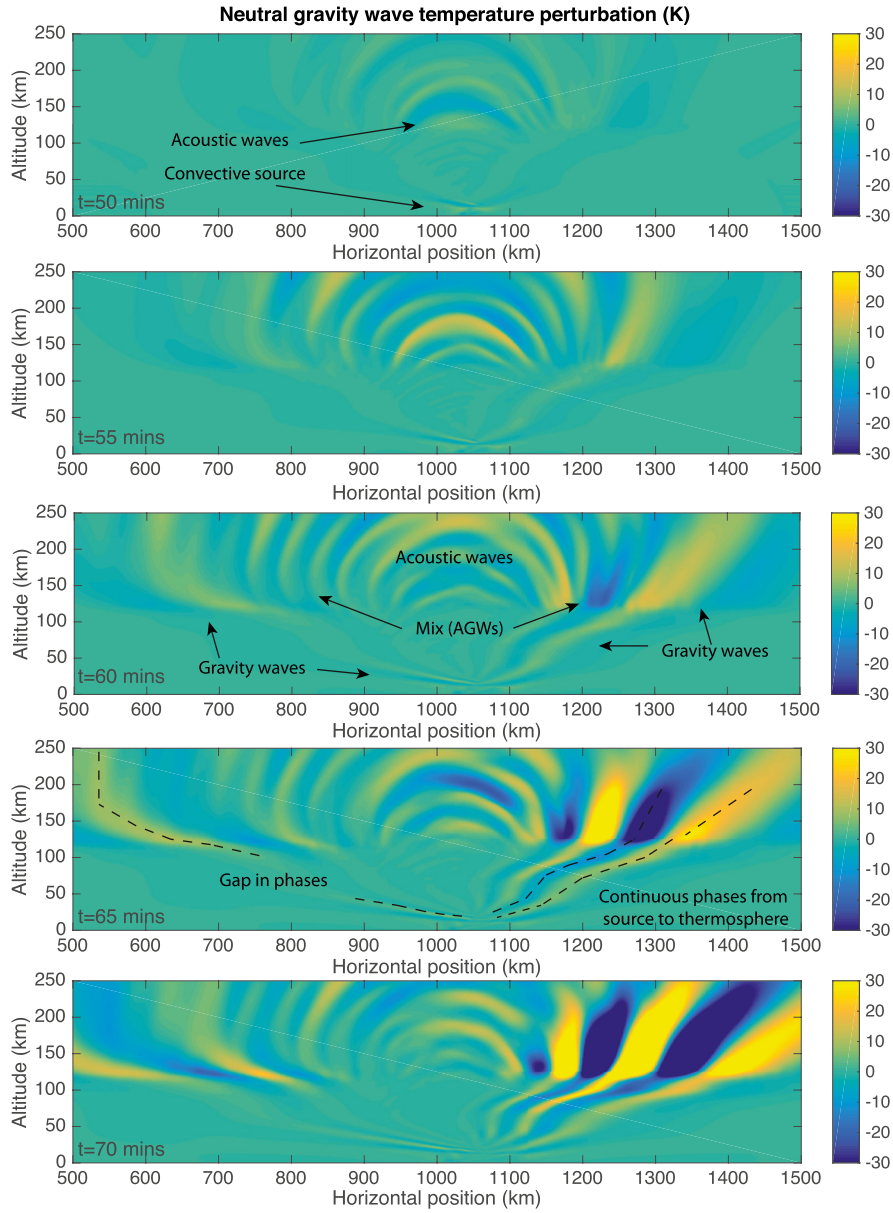

Figure 4. A time sequence of the gravity wave temperature perturbation between $t = 50$ and 70 min consisting of only primary acoustic and gravity waves. The colorbars are saturated at $t = 65$ and 70 min in order to show the waves in the lower atmosphere as well as those in the thermosphere.

3.1.2. Primary Wave Phase Speeds

To analyze the primary wave spectra, a zonal-time slice of the simulation is taken at 80, 120, and 240 km altitude and is displayed in Figures 5a–5c, respectively. The ground relative phase speeds are measured directly from the plot by following the peaks of the waves over time. As before, the analysis is limited to times before $t = 80$ min to exclude the influence of secondary waves. We recall that theoretical phase speed limits discussed in Section 2.2 suggest that eastward propagating waves primary waves should not exceed 170 m/s above 62 km altitude, and westward waves should not exceed 210 m/s above 75.5 km.

At 80 km altitude, Figure 5a shows only eastward propagating waves with phase speeds ranging from ∼76 to 125 m/s. The lack of westward propagating waves at this altitude is likely due to a combination of (a) source spectrum differences, (b) critical level filtering on westward waves in the stratosphere, and (c) local minima in the

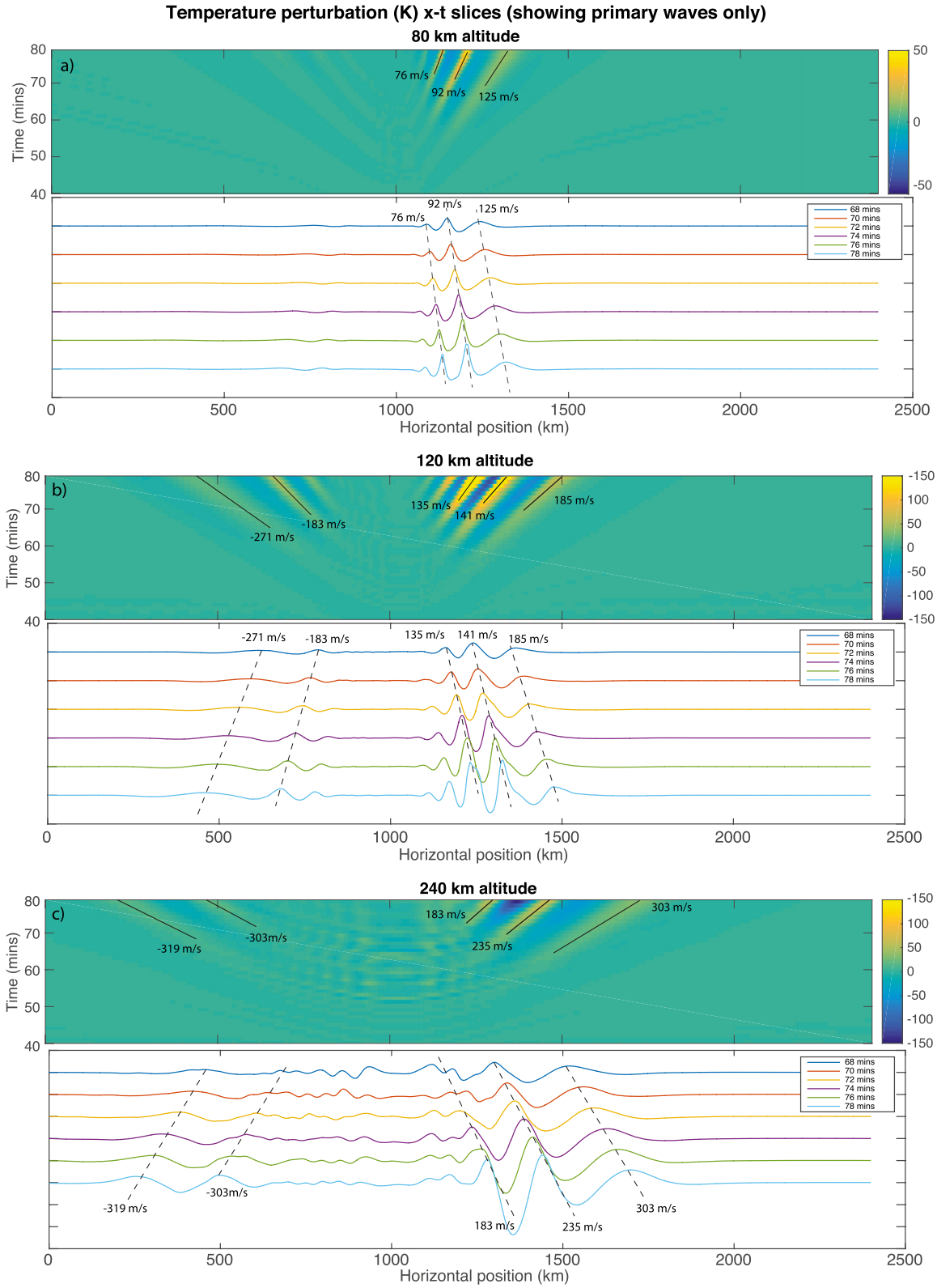

Figure 5. Slices of the neutral temperature perturbations (zonal-t) at (a) 80, (b) 120, and (c) 240 km altitude, showing primary waves only.

allowable maximum phase speed around 80 km altitude. We note that the waves are already becoming nonlinear at this altitude and wave-mean flow interactions are shifting these waves to higher phase speeds.

At z = 120 km, both eastward and westward propagating waves are present, but with different ground relative phase speeds and amplitudes. The eastward waves are stronger in amplitude than the westward waves but have slower ground relative phase speeds. The eastward propagating waves have dominant ground relative phase speeds from 135 to 185 m/s and the westward waves have speeds of 183–271 m/s. These phase speeds at least partially exceed the conditions set for the maximum phase speeds that can pass from the mesosphere to the thermosphere (should not exceed 170 m/s above 62 km altitude for eastward or 210 m/s above 75.5 km for westward waves, as described in Section 3), however these waves are clearly primary waves that originated from the tropospheric source

At z = 240 km, an altitude which is representative of the bottom part of ionospheric F layer, we find eastward waves with phase speeds from 183 to 303 m/s and westward waves from 303 to 319 m/s. These waves violate the maximum phase speeds that should be able to pass mesopause region, but are consistent with phase speeds of MSTIDs seen in ionospheric measurements (Azeem et al., 2017; Chou et al., 2017; Figueiredo et al., 2018; Nicolls et al., 2014; Röttger, 1977; Vadas & Crowley, 2010; Xu et al., 2019). The analyses presented in Vadas and Crowley (2010) and Vadas and Azeem (2021) would conclude that these waves must be secondary waves generated in the thermosphere, whereas, in fact, these waves are primary waves originating in the source region. In the next section, we explore the mechanisms that allow this

3.1.3. Analysis of the Origin of the Waves at 240 km

In this subsection, we investigate the characteristics of the waves at z = 240 km in details and demonstrate that waves with phase speeds greater than the bottleneck speed can pass from the lower atmospheric source region to the thermosphere. We begin by performing a Morlet wavelet analysis (Torrence & Compo, 1998) on the waves at z = 240 km and t = 78 min to measure the horizontal wavelengths as a function of zonal position. Figure 6 shows that the dominant eastward waves have horizontal wavelengths ranging from ∼173 to 245 km, and the westward waves have horizontal wavelengths ranging from 238 to 262 km. These are also consistent with typical detected MSTID wavelengths in the ionosphere (Azeem et al., 2017; Chou et al., 2017; Hunsucker, 1982; Röttger, 1977; Vadas & Crowley, 2010; Xu et al., 2019). Vadas and Azeem (2021) and Vadas et al. (2009) suggested that for a point source generation of GWs, the horizontal wavelength should increase quadratically with radius from the source. Our result appears to be roughly consistent with this prediction, with the caveat that we are not using a point source but a compact line source, which exhibits different geometric dispersion.

We choose to focus on the fastest wave seen in Figure 5c, which is the westward propagating mode with a ground relative phase speed of 319 m/s, as this is the most extreme case. At t = 78 min, the 319 m/s westward wave is located at a zonal position of x = 252 km, which corresponds to a dominant horizontal wavelength of 262 km. This implies a ground relative period (λ/C_p) of 13.7 min. We then use the horizontal wavelength and period, along with the ambient winds and buoyancy frequency, in the gravity wave dispersion relation to predict the vertical wavelength with altitude:

$$m^2 = \frac{k^2 N^2}{(\omega - kU)^2} - k^2 - \frac{1}{4H^2} \tag{6}$$

where m is the vertical wavenumber, k is the horizontal wavenumber, N is the buoyancy frequency, ω is the ground relative frequency, and H is the scale height (RT/g). The predicted vertical wavelength ($2\pi/m$) is plotted in Figure 7 and shows regions of propagation between 30 and 50 km altitude and above 105 km altitude with a 56 km deep evanescent region in between. The prediction in Figure 7 is consistent with both the simulation results in Figure 4, which shows a gap in the wave phase between 50 and 105 km, and the phase speed limits in Figure 3. Therefore, these predictions align with the analysis in Vadas and Crowley (2010) that this wave should not be able to reach the thermosphere from the source, yet it does.

This is because the vertical wavelength in the propagating region (30–50 km) is 242 km, which is very large compared to the depth of the evanescent region (approximately 1/5 of the vertical wavelength) so the wave is able to tunnel through the mesosphere and reappear as a propagating wave in the thermosphere. This effect was discussed and demonstrated in Gavrilov and Kshevetskii (2018), who simulated the propagation of a wave that is supersonic at the source region but tunnels through the atmosphere and appears as a propagating wave in the

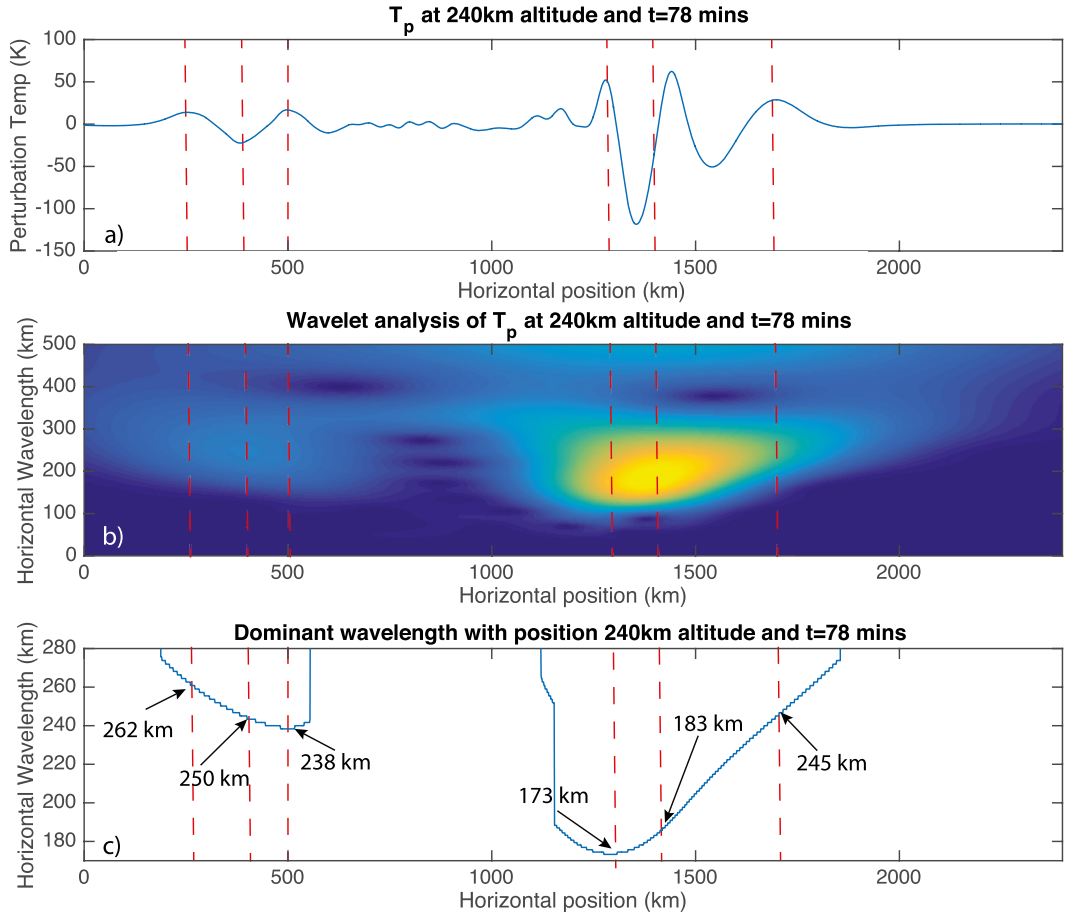

Figure 6. (a) Gravity wave perturbation temperature at $z = 240$ km and $t = 78$ min, (b) Wavelet analysis of the horizontal wavelength as a function of position, (c) the dominant horizontal wavelength at each horizontal position.

thermosphere. Inchin et al. (2020) also demonstrated that gravity waves excited by moving source at the ground level (representing tsunami propagation) with horizontal speed of ~270 m/s can also tunnel through lower atmosphere and become propagating in the thermosphere. R. L. Walterscheid and Hecht (2003) presented a theoretical examination of the propagation, energetics, responsivity and coupling of evanescent acoustic-gravity waves, suggesting that the importance of tunneling may be substantially underestimated.

We show a demonstration of this effect by performing an additional simulation, using the same ambient atmosphere as before, but with a simple quasi-monochromatic wave vertical body forcing (with a horizontal wavelength of 262 km, and a period of 13.7 min) in place of the more spectrally rich thunderstorm source. The complete forcing is:

$$F(x,\ z,\ t) = A_m \cdot \exp\left[-\frac{(x-x_c)^2}{2\sigma_x^2} - \frac{(z-z_c)^2}{2\sigma_z^2} - \frac{(t-t_c)^2}{2\sigma_t^2}\right] \cdot \cos(\omega(t-t_c) - k(x-x_c)) \quad (7)$$

where $A_m = 0.0001$ m/s, $k = -2\pi/262$ km, $x_c = 1040$ km, $\sigma_x = 131$ km, $z_c = 7$ km, $\sigma_z = 3$ km, $\omega = 2\ \pi/13.7$ min, $t_c = 65$ min, $\sigma_t = 13.7$ min. Note, the amplitude is kept very low to limit any nonlinear effects. Figure 8 shows (a) the temperature perturbation (from ground to $z = 250$ km altitude), (b) density scaled temperature perturbation (from ground to 120 km altitude), and (c) the vertical forcing for the quasi monochromatic forcing simulation from $t = 60$–100 min. The raw temperature perturbations in Figure 8a simply shows a westward propagating wave above 105 km altitude, just like in the thunderstorm simulation. However, once the results are density scaled (Figure 8b), this wave can clearly be seen tunneling from the source region to the stratospheric propagating region (between 30 and 50 km altitude) and then tunneling again up to 105 km altitude (with reflection at the evanescent boundaries). This is consistent with the predicted vertical wavelength analysis in Figure 7.

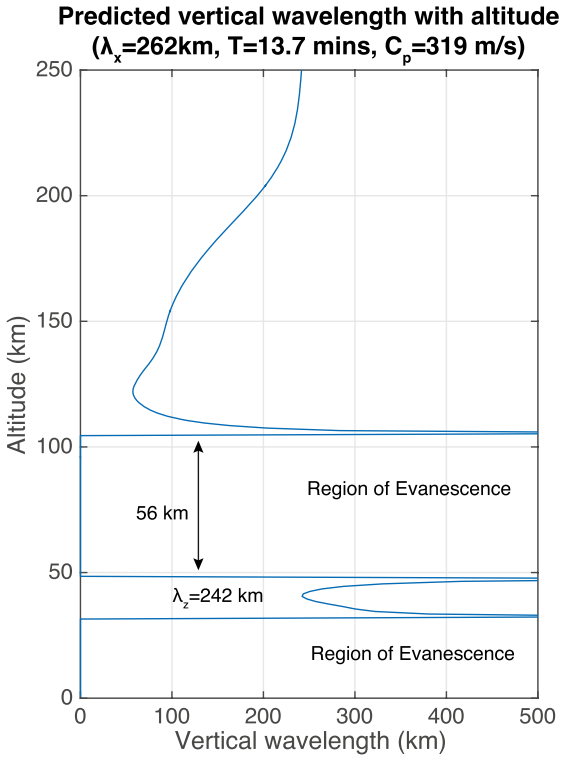

Figure 7. Predicted vertical wavelength with altitude for a westward propagating gravity wave with a horizontal wavelength of 262 km and a period of 13.7 min.

The simulation shows that the waves, even at small forcing amplitudes, successfully tunnel into the thermosphere and F-region altitudes, despite the restrictions suggested by linear theory and Vadas and Crowley (2010). Therefore, it is suggested that waves in the F region, that have a phase speed greater than the imposed limit in the lower/middle atmosphere, can originate from a tropospheric source. That is not to say that waves seen in the F-region don't also originate from wave breaking in the thermosphere or upper mesosphere but are, in most realistic cases, a combination of primary and secondary waves.

3.2. Secondary Wave Response

In this section, we examine the secondary wave response from the breaking primary waves and nonlinear mechanisms. The initial breaking of the primary waves and the early evolution of the subsequently generated secondary waves are shown in Figure 9. Breaking occurs after $t = 80$ min for the eastward propagating primary waves and ~100 min for the westward propagating primary waves. The eastward waves break between 65 and 140 km altitude with larger and more energetic eddies at higher altitudes (see the black dotted lines in Figure 9 panel a). This wave breaking generates a broad range of fast secondary acoustic and gravity waves that propagate, in both directions, away from the source of the breaking. The westward propagating secondary waves that emanate from the breaking region are particularly evident and are highlighted in Box 1. The eastward propagating secondary waves are more difficult to clearly identify as the overlap with the strongly nonlinear primary waves and turbulent structure. In addition, as the primary eastward waves becomes strongly nonlinear, they deposit part of their momentum and energy into the local ambient flow which can "self-accelerate" the wave (and affect subsequent waves) (Lund & Fritts, 2012; Fritts et al., 2015; Dong et al., 2020;

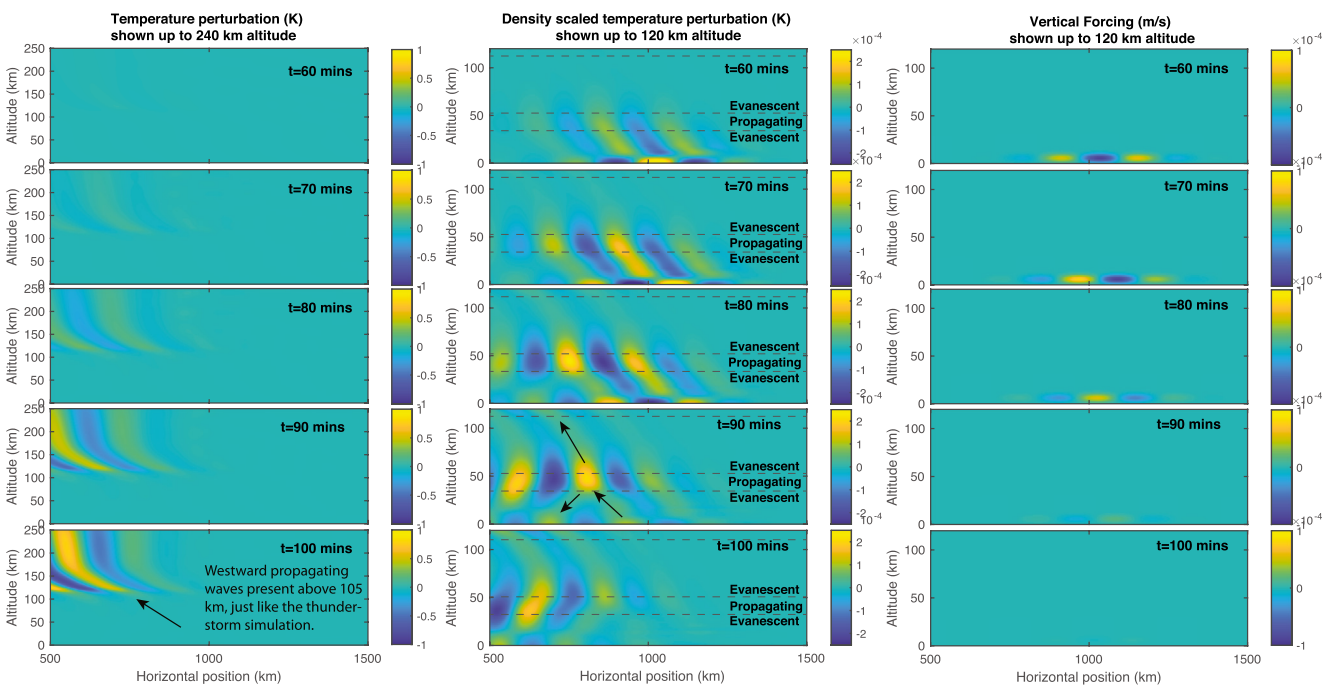

Figure 8. (a) The gravity wave temperature perturbation, (b) density scaled gravity wave perturbation, and (c) the vertical forcing for the quasi monochromatic forcing simulation.

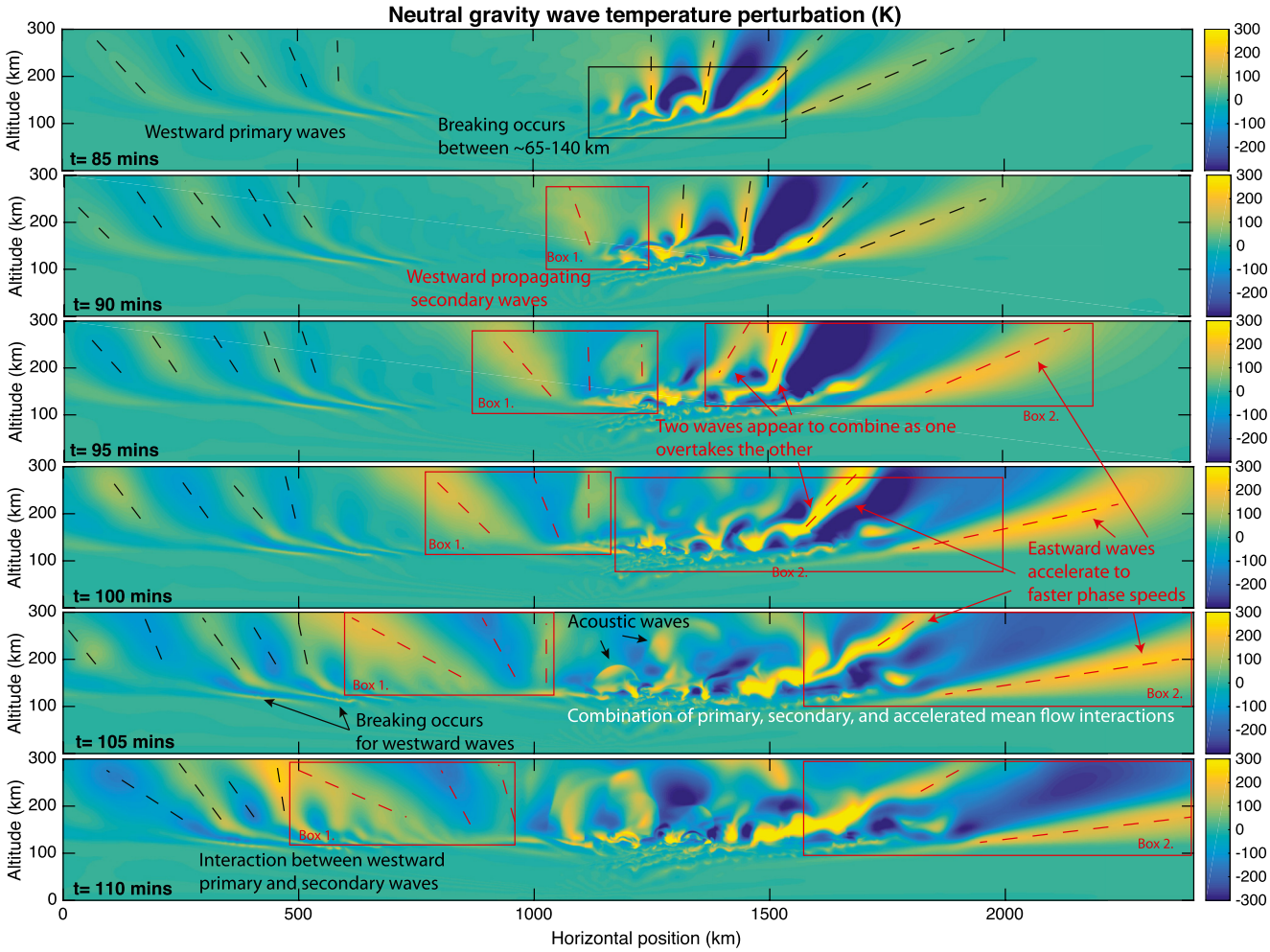

Figure 9. A time sequence of the gravity wave temperature perturbation between $t = 85$ and 110 min showing the breaking of the primary gravity waves and generation of secondary waves. Black dotted lines indicate the breaking/self-accelerated primary waves, red dotted lines indicate secondary waves or the primary waves after they have been significantly accelerated by wave-mean flow interactions.

Fritts et al., 2020), changing its intrinsic frequency and accelerating its phase speed. The mean flow acceleration associated with the breaking waves in the thermosphere can lead to feedback where subsequent waves are refracted to smaller vertical wavelengths, break, and induce further mean flow acceleration. This leads to increasingly sharp local wind shears that can ultimately form a critical level for upward propagating waves (Lund & Fritts, 2012). This particularly affects the eastward propagating waves highlighted in Box 2 (red lines) which, kink, break, and then accelerate significantly between $t = 95$ and 110 min and are refracted to much larger horizontal wavelengths. Typically, the deposition of wave energy and momentum is assessed through the analysis of the wave stress divergence (Vadas et al., 2019; Heale, Bossert, et al., 2020; Zhou et al., 2002; J. B. Snively, 2017; Franke & Robinson, 1999; Zhou et al., 2002; Chun & Kim, 2008). The secondary waves superpose and interact with both the eastward and westward propagating primary waves and primary waves that have been self-accelerated or modified by wave-flow interactions. This leads to a mixed wave spectra in the thermosphere. The waves that can be linked to/originate from primary wave structures and self-accelerated primary waves are shown with dotted black lines. Secondary waves, and/or waves significantly altered by acceleration as a result of wave-flow interactions are shown with red dotted lines. One such overlapping and interaction of secondary waves with accelerated primary waves can be seen between 95 and 100 min in Box 2. Two phases, indicated by two red dotted lines at $t = 95$ min, become one single red-dotted line at $t = 100$ min as the faster mode generated by the wave breaking combines with a slower mode further to the east, which then accelerates beyond 100 min.

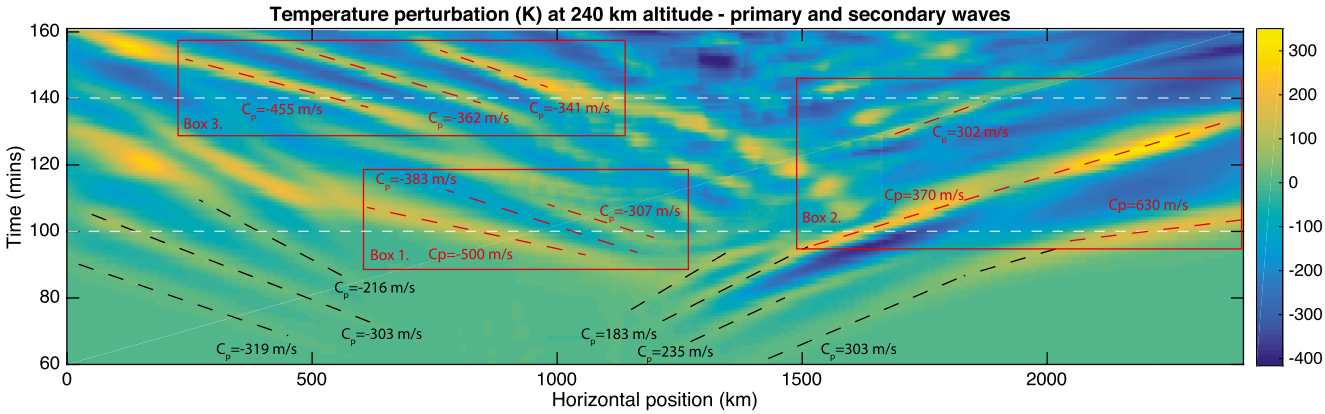

Figure 10. Slices of the neutral temperature perturbations (zonal-time) at 240 km altitude, showing primary waves (black dotted), secondary (red dotted) waves. Dotted white lines indicate the horizontal slices taken at $t = 100$, and 140 min which are shown in Figures 11 and 12 respectively.

As with the primary waves, we take a zonal—time slice at $z = 240$ km in order to assess the phase speeds of the neutral AGWs at F-region heights, which are shown in Figure 10. As with Figure 9, dotted black lines indicate primary waves, red lines indicate secondary waves or accelerated/nonlinearly altered waves.

Figure 10 shows that secondary waves are notably present after ~85 min and are most evident for their westward propagation (Boxes 1 and 3). The secondary waves in Box 1 are the westward propagating waves annotated with red lines in Figure 9. They originate around 90 min, × ~1,200 km, and $z \sim 140$ km and are generated by localized breaking of the eastward primary waves. The phase speeds range from 300 to 500 m/s and are faster than the primary wave spectra and are certainly acoustic-gravity waves at the higher phase speeds, but there is overlap between the primary and secondary wave spectra in the low 300 m/s phase speed range. These results are similar to Vadas and Crowley (2010) who found phase speeds of 100–600 m/s for secondary waves above convection, noting that the spectra peaks between 100 and 300 m/s. However, we cannot clearly identify propagating secondary waves at the slower phase speeds (less than 300 m/s) suggested by Vadas and Crowley (2010). The westward primary and secondary waves overlap and interact beyond 110 min, at horizontal positions less than $x = 500$. Box 3 also shows a clear spectra of westward propagating secondary waves that increase ~ quadratically in phase speed (from 340 to 455 m/s) with decreasing x (increasing westward direction). This is in contrast to Vadas et al. (2019)'s description of a secondary wave generated by a point source, which suggested the phase speed should increase linearly with distance. This suggests significant nonlinearity of the waves and/or multiple sources. Eastward propagating large amplitude waves are clearly present beyond 130 min at $x > 1{,}500$ km (Box 2). Some of these waves appear connected in phase to the primary waves but have significantly faster phase speeds. For example, primary waves that initially have phase speeds of 183 and 303 m/s appear to transition to much larger phase speeds of 370 and 630 m/s, respectively (box 2). This effect is caused in a large part by a combination of wave self-acceleration, wave-wave, and wave-flow interactions. As the primary waves become strongly nonlinear they deposit some of their energy and momentum into the background flow locally. This temporal change in the background flow acts to subsequently accelerate the wave itself, shifting it to faster phase speeds (Dong et al., 2020; Fritts et al., 2015; Fritts et al., 2020; Lund & Fritts, 2012). In addition, the accelerated waves are superposed with fast propagating secondary acoustic-gravity waves generated by primary wave breaking between $x = 1{,}300$–$1{,}400$ km. Beyond $t = 120$ min, the majority of the waves are secondary waves generated by wave breaking. Note that the secondary waves in Boxes 1 and 2 correspond to the propagating secondary waves highlighted with red lines in Figure 9.

We note that even in this relatively idealized simulation, it is still difficult to clearly separate the primary and secondary waves. In this case, there are many localized forcing centers that result from the primary wave breaking and dissipation which lead to multiple secondary waves sources which nonlinearly interact and superimpose to give a composite spectrum of secondary waves. This is complicated by self-acceleration of the primary waves themselves which are transformed to higher different phase speeds than they originally possessed.

In order to examine the horizontal wavelengths of the secondary waves in Boxes 1–3, we take a horizontal slice through Figure 10 at $t = 100$ and 140 min and perform a wavelet analysis. Figure 11 shows the horizontal slice

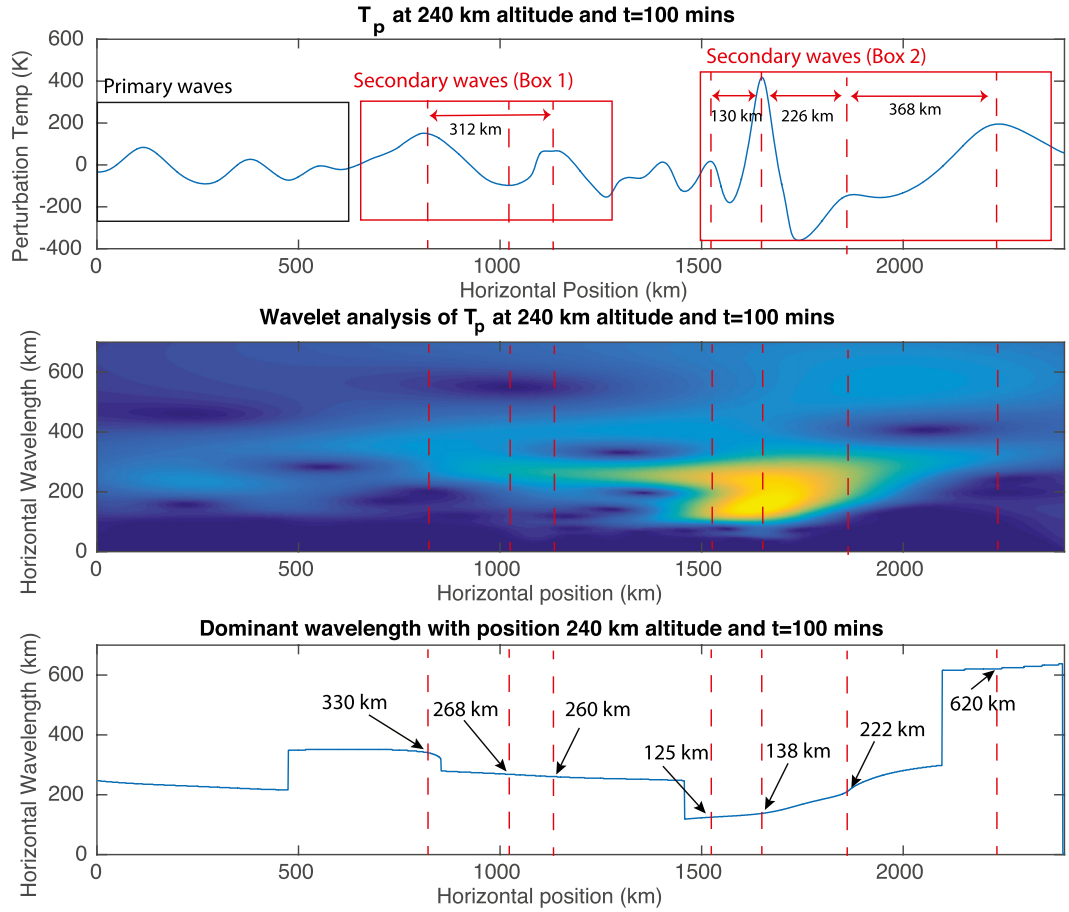

Figure 11. (Ea) Gravity wave perturbation temperature at $z = 240$ km and $t = 100$ min, (b) Wavelet analysis of the horizontal wavelength as a function of position, (c) the dominant horizontal wavelength at each horizontal position.

and measured wavelength's at $t = 100$ min. The waves highlighted by the black box are the westward propagating primary waves that are also seen in Figure 6.

The westward propagating secondary waves (Box 1) show two peaks in temperature which are separated by 312 km. However, these waves are asymmetric in nature and are not sinusoidal like the primary waves, suggesting a rich spectral content arising from superposition of waves, wave-mean flow interactions, and wave-wave interactions. The dominant wavelength (as suggested by the wavelet analysis) increases from 260 km at the right most temperature peak in Box 1 ($x \sim 1{,}200$ km) to 330 km at the leftmost temperature peak ($x \sim 800$ km) which includes a step increase in the dominant wavelength at ~820 km suggestive of a separate mode. Clearly, due to the rich spectral content, measurements of the wavelengths from wavelet analysis and the peak to peak wavelength do not necessarily agree because the wavelet analysis, which is measuring the wavelength at a point location by convolving the signal with a wavelet. Therefore, the steepness and asymmetry of the signal can influence the wavelength measurement complicating spectral analysis.

For the eastward propagating waves (Box 2), there are two distinct wave packets. The first packet dominates between $x = 1{,}500$ and 1,800 km, with the wavelength increasing from 125 to 225 km over that range. The second packet has a much larger wavelength of 620 km and dominates beyond $x \sim 2{,}100$ km. Between $x = 1{,}800$ and 2,100 km, the spectrum is a mixture of two packets. This highlights the complex nature of secondary wave generation and the spectra being a mixture of interacting primary wave, secondary waves, breaking structure and induced larger-scale flows.

Figure 12 shows the horizontal slice and measured wavelength's at $t = 140$ min. The westward propagating waves in Box 3 are extremely steep (we note that the 2D simulation overestimates wave amplitudes) with three

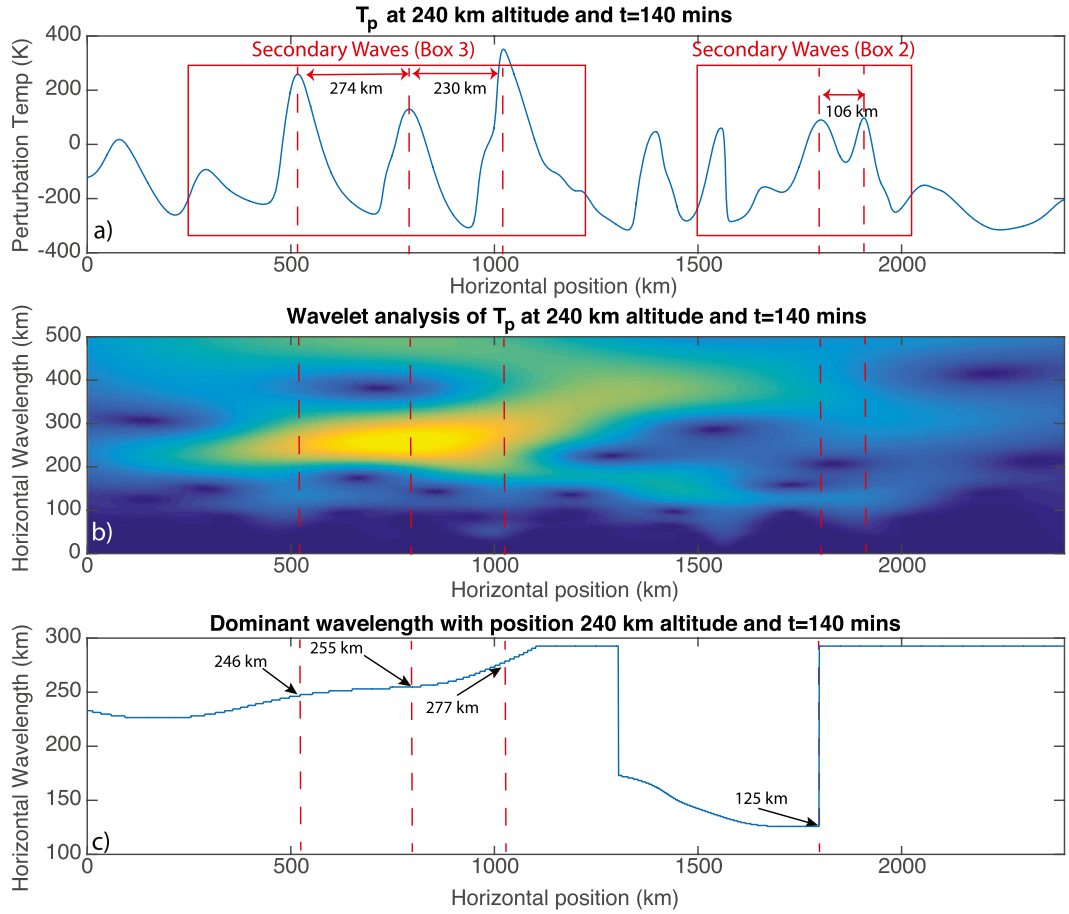

Figure 12. (a) Gravity wave perturbation temperature at $z = 240$ km and $t = 140$ min, (b) Wavelet analysis of the horizontal wavelength as a function of position, (c) the dominant horizontal wavelength at each horizontal position.

distinct peaks. The peak to peak distances are 230 and 274 km respectively, with the wavelength increasing in the westward direction (as x decreases). However, the wavelet analysis suggests that the wavelength increases in the eastward direction from 246 to 277 km. This discrepancy occurs because the eastward most peak in Box 3 is wider than the westward most peak (so a convolution method such as a wavelet analysis measures a larger local wavelength), but the distance between the peaks increases in the westward direction. Once again, this highlights the nonlinearity of these waves.

The eastward propagating waves show two distinct packets. The smaller scales range between 100 and 200 km with a peak to peak measurement of 106 km in Box 2. These smaller scales are superimposed on the larger-scale packet which ranges between 300 and 400 km in horizontal wavelength.

3.3. The Effect of Thunderstorm Source Amplitude

It is also key to note that nonlinear effects such as the wave breaking, self-acceleration, wave-wave, and wave-flow interactions are exacerbated by overestimated amplitudes as a result of performing a 2D simulation versus full 3D. As previous mentioned, Dong et al. (2020) and Fritts et al. (2020) noted that 2D simulations exhibited stronger secondary AGW responses than in 3D and that instabilities decayed more rapidly when 3D breaking is permitted. To understand the extend of these effects, we also ran simulations with forcing strengths that are a 1/4 the amplitude, and 1/100th the amplitude of the original simulation. While this does not mitigate for the lack of realistic 3D turbulent evolution, it does reduce nonlinear effects such as wave-wave, and wave-mean flow interactions. Figure 13 presents the zonal—time slice at $z = 240$ km for the two reduced amplitude simulations for comparison with Figure 10.

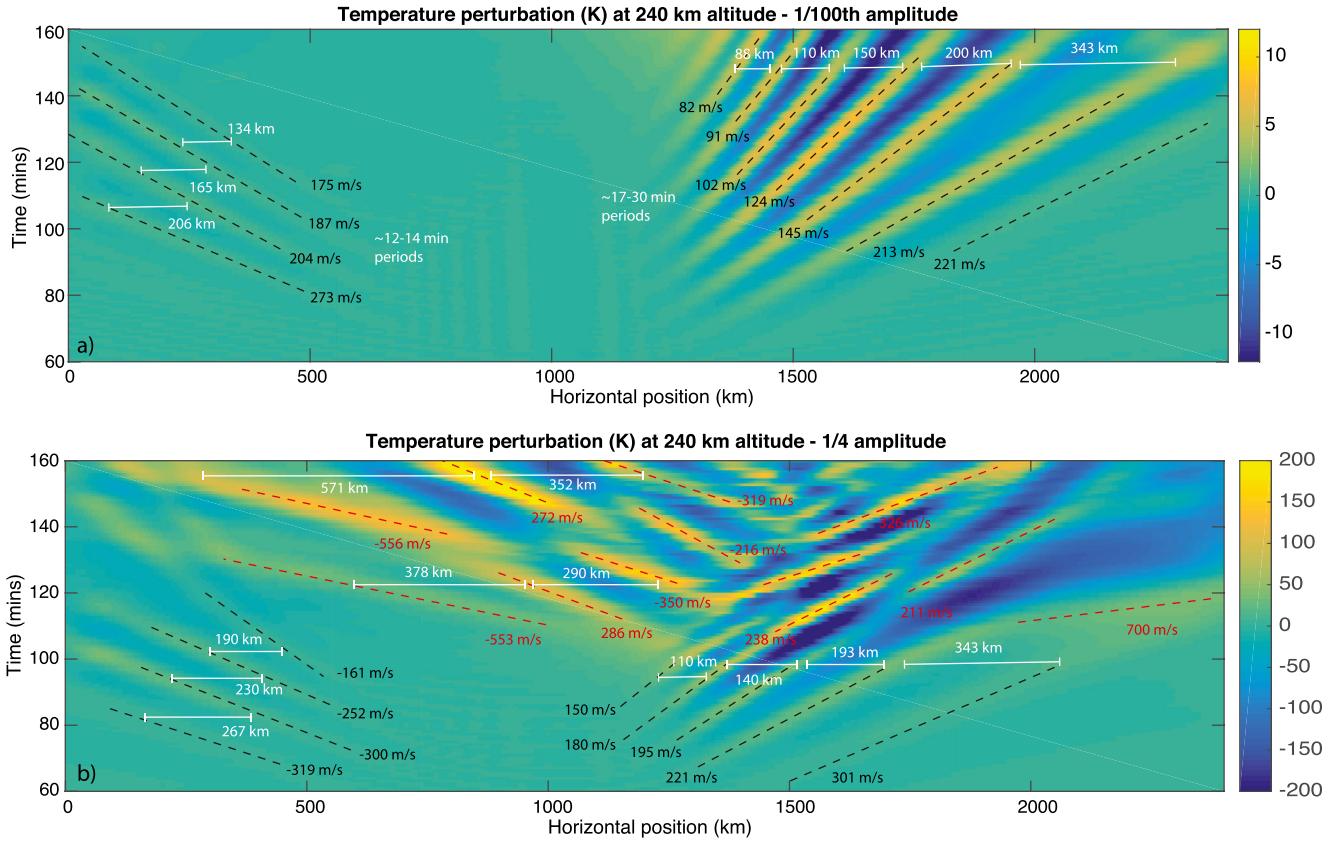

Figure 13. Slices of the neutral temperature perturbations (zonal-time) at 240 km altitude (a) the 1/100th amplitude case and (b) the 1/4 amplitude case, showing primary waves (black dotted), secondary/accelerated (red dotted) waves.

The waves in the 1/100th amplitude case (Figure 13a) do not break at all in the thermosphere and represent a quasilinear simulation. As a result, a full spectrum of primary waves can be seen. The wave spectra is broader, and the phase speeds are generally lower, than the full amplitude case due to reduced nonlinear effects. For the eastward propagating waves, the phase speeds range from 80 to 221 m/s (compared with 183–303 m/s in the full amplitude case) with the largest amplitude wave having a phase speed of 124 m/s and little evidence of strong self-acceleration in this case. For the westward propagating primary waves, the phase speeds range from 175 to 273 m/s (compared to 216–319 m/s for the full amplitude case). The horizontal wavelengths range from 88 to 343 km and the periods between 12 and 30 min. We note that the primary waves with slower phase speeds (and shorter horizontal wavelength) appear at later times in the 1/100 amplitude simulation (after 100 min). In the full amplitude case, the wave field has already become strongly nonlinear and the waves have undergone breaking by 100 min. This obscures detection of the slower phase speed primary waves that reach the thermosphere at later times and accelerates the waves that are already present to faster phase speeds. Also, the stronger source in the full amplitude case puts more energy into the higher phase speed modes, thus they have higher amplitudes when they reach the thermosphere. It is also key to note that the primary wave phase speeds seen in the 1/100 amplitude case still exceed the theoretical upper limits set in the mesosphere. The horizontal wavelengths also change with time due to dispersion of the wave packet.

In the 1/4 amplitude case (Figure 13b), the primary wave spectra is very similar to the full amplitude case but with smaller amplitudes. As a result of the smaller amplitudes, the wave become strongly nonlinear and break ~10–15 min later than in the full amplitude case. This allows some of the slower phase speed primary waves to reach the thermosphere before the wave field becomes nonlinear and breaking occurs. The lower amplitudes of the waves in the 1/4 amplitude case mean that self-acceleration and wave-flow interactions are generally weaker. The phase speeds for the secondary waves are also similar to the full amplitude case but with a broader range (i.e., from the low 200 m/s up to 700 m/s). In this case, the lower end of the secondary phase speed range noted in Vadas and Crowley (2010) is present, but is not in the full amplitude case. We note the speed of sound at

Table 1
Comparison of Traveling Ionospheric Disturbances (TIDs)/Gravity Waves (GWs) Parameter Ranges at F Regions Heights

Study	Horizontal wavelength (km)	Period (min)	Phase speeds (m/s)
This paper (full amp)	130–620	11–21	183–630
This paper (1/4 amp)	110–570	10–33	150–700
This paper (1/100th amp)	88–343	12–30	82–273
Vadas and Crowley (2010)	100–3,000	15–90	100–650
Vadas et al. (2019)	170–1,850	11–54	245–630
Vadas and Azeem (2021)	100–500	8–40	150–530
Azeem et al. (2017)	150–400	14–30	180–260
Xu et al. (2019)	250–350	15–60	100–200
Chen et al. (2019)	200–450	20–50	120–220
Figueiredo et al. (2018)	452 ± 107	24 ± 4	323± 81
Kotake et al. (2007)	100–350	20–45	60–180
Otsuka et al. (2011)	100–600	N/A	80–180
Paulino et al. (2016)	100–200	10–35	30–180
Chou et al. (2017)	160–270	15–22	161–200
Nicolls et al. (2014)	70–500	25–60	>100–150

this altitude is 735 m/s so the fastest waves present are approaching acoustic speeds. The eastern most wave in this case has a 700 m/s phase speed (vs. 630 m/s in the full amplitude simulation), but self-acceleration effects are weaker than the full amplitude case. It is therefore suggested that this wave is a very fast eastward propagating secondary acoustic-gravity wave that is generated by primary wave breaking. This case shows some of the complexity in identifying strict secondary waves from primary waves or waves that have undergone self-acceleration or have be modified by mean flow acceleration and momentum deposition into the background flow.

From this comparison, it is clear that the amplitude of the initial source can have a significant influence on both (a) the spectra of the waves that are observed in the thermosphere and (b) the strength of nonlinear/self-acceleration effects created by that wave spectra. In future, we shall perform a full 3D case with the same source. However, even in the smallest amplitude case, fast primary wave phase speeds are able to propagate into the thermosphere. This comparison also shows how dramatically different the wave field is when comparing quasi-linear and fully nonlinear evolution.

4. Summary and Conclusions

In this study, we used a 2D fully compressible nonlinear model to simulate the gravity wave response to a single convective plume and assessed the primary and secondary gravity wave spectra at F-regions altitudes. The convective plume had a zonal half width of 6 km and a period of 20 min.

We found that the eastward propagating primary waves break first in the Mesosphere and Lower Thermosphere (MLT) ∼45 min after the peak in the latent heat release by the convective plume. The westward primary waves break about 15 min later. The breaking and wave dissipation generates secondary westward and eastward propagating acoustic, acoustic-gravity and gravity waves that interact with the primary waves and the mean flow. The interaction between the wave packet and the accelerated local flow around the packet can also cause significant acceleration of the primary waves which are then shifted to faster phase speeds. However, such effects can be reduced in 2.5 and 3D simulations, due to the spatial isolation of wave packets (Dong et al., 2020; Fritts et al., 2020).

At 240 km altitude (taken at a proxy for F-region heights), we found that westward propagating primary waves had phase speeds ranging from 216 to 319 m/s and dominant horizontal wavelengths ranging from 238 to 262 km and inferred periods of ∼13–15 min, while the eastward propagating primary waves had phase speeds ranging from 183 to 303 m/s, dominant wavelengths of 173–245 km, and inferred dominant periods of 13–16 min.

Even in this relatively simplified case, delineating the secondary waves from the primary waves and the turbulent structure is challenging. The secondary wave spectra is broad and there is an overlap with the primary wave spectra. However, we found that the dominant secondary waves generally had faster phase speeds than the primary waves. We identified three particular regions of secondary waves and found that the eastward secondary waves had phase speeds from 300 to 630 m/s, dominant wavelengths between 130 and 620 km, implying periods of ∼10–21 min. Westward propagating secondary waves had phase speeds from 307 to 500 m/s, dominant wavelengths between 230 and 312 km, implying periods of ∼11–17 min Table 1 provides a comparison of our the range of results with other observational studies.

We also note that the amplitude of the source can dramatically affect the observed phase speed spectra of both the primary and secondary waves in the thermosphere. A larger amplitude source tends toward faster primary waves, longer dominate wavelengths, and a decrease in the presence of slower secondary waves. This is primarily because (a) larger amplitudes of the primary waves in the thermosphere lead to stronger wave-flow interactions and self-acceleration which increases the phase speeds of waves even further (b) more energy goes into the faster phase speed modes, and (c) larger amplitude waves obtain saturation and break more rapidly, obscuring the

presence of slower phase speed waves as the wave field becomes strongly turbulent. These results also highlight the vast differences in the wave field under quasilinear and fully nonlinear limits.

Theoretical upper limits have been proposed on the gravity wave phase speeds that can pass from the mesosphere to the thermosphere and, on that basis, previous research has suggested that observed TIDs with phase speeds that exceed this upper limit must result from secondary gravity waves generated by primary wave breaking in the thermosphere (Vadas & Azeem, 2021; Vadas & Crowley, 2010; Vadas et al., 2019). Here, we have demonstrated that primary waves with phase speeds that exceed this theoretical upper limit can propagate from the source to ionospheric heights, consistent with prior predictions by, for example, R. L. Walterscheid and Hecht (2003) and Gavrilov and Kshevetskii (2018). These waves have large vertical wavelengths and are able to tunnel through large portions of the lower atmosphere and emerge as a propagating wave in the thermosphere. Thus, it cannot be reliably assumed that TIDs may be separated as being due to primary or secondary AGWs simply based on this proposed upper limit. Nevertheless, secondary waves will tend toward higher phase speeds than the primary waves at F-region altitudes.

Data Availability Statement

Simulation data will be made available at https://doi.org/10.528 1/zenodo.5597 891.

Acknowledgments
Research by Christopher Heale was carried out under NSF-grant AGS-1822 551. Research by Paul Inchin and Jonathan Snively was carried out under NASA grant 80NSSC18K1037. The authors thank the editor and two reviewers for their time and effort in improving this manuscript.

References

Amorim, D. C. M., Pimenta, A. A., Bittencourt, J. A., & Fagundes, P. R. (2011). Long-term study of medium-scale traveling ionospheric disturbances using O I 630 nm all-sky imaging and ionosonde over Brazilian low latitudes. *Journal of Geophysical Research*, *116*(A6). https://doi.org/10.1029/2010ja016090

Azeem, I., & Barlage, M. (2018). Atmosphere-ionosphere coupling from convectively generated gravity waves. *Advances in Space Research*, *61*(7), 1931–1941. https://doi.org/10.1016/j.asr.2017.09.029

Azeem, I., Vadas, S. L., Crowley, G., & Makela, J. J. (2017). Traveling ionospheric disturbances over the United States induced by gravity waves from the 2011 Tohoku tsunami and comparison with gravity wave dissipative theory. *Journal of Geophysical Research: Space Physics*, *122*(3), 3430–3447. https://doi.org/10.1002/2016ja023659

Azeem, I., Yue, J., Hoffmann, L., Miller, S. D., Straka, W. C., III, & Crowley, G. (2015). Multisensor profiling of a concentric gravity wave event propagating from the troposphere to the ionosphere. *Geophysical Research Letters*, *42*(19), 7874–7880. https://doi.org/10.1002/2015gl065903

Bale, D. S., LeVeque, R. J., Mitran, S., & Rossmanith, J. A. (2002). A wave propagation method for conservation laws and balance laws with spatially varying flux functions. *Journal of Scientific Computing*, *24*(3), 955–978.

Behnke, R. (1979). F layer height bands in the nocturnal ionosphere over Arecibo. *Journal of Geophysical Research*, *84*(A3), 974–978. https://doi.org/10.1029/ja084ia03p00974

Bossert, K., Kruse, C. G., Heale, C. J., Fritts, D. C., Williams, B. P., Snively, J. B., et al. (2017). Secondary gravity wave generation over New Zealand during the deepwave campaign. *Journal of Geophysical Research: Atmospheres*, *122*(15), 7834–7850. https://doi.org/10.1002/2016jd026079

Chen, G., Zhou, C., Liu, Y., Zhao, J., Tang, Q., Wang, X., & Zhao, Z. (2019). A statistical analysis of medium-scale traveling ionospheric disturbances during 2014–2017 using the Hong Kong CORS network. *Earth Planets and Space*, *71*(1), 52. https://doi.org/10.1186/s40623-019-1031-9

Chou, M.-Y., Lin, C. C. H., Yue, J., Chang, L. C., Tsai, H.-F., & Chen, C.-H. (2017). Medium-scale traveling ionospheric disturbances triggered by Super Typhoon Nepartak (2016). *Geophysical Research Letters*, *44*(15), 7569–7577. https://doi.org/10.1002/2017gl073961

Chun, H.-Y., & Kim, Y.-H. (2008). Secondary waves generated by breaking of convective gravity waves in the mesosphere and their influence in the wave momentum flux. *Journal of Geophysical Research*, *113*(D23). https://doi.org/10.1029/2008jd009792

Cosgrove, R. B., & Tsunoda, R. T. (2004). Instability of the e-f coupled nighttime midlatitude ionosphere. *Journal of Geophysical Research*, *109*(A4). https://doi.org/10.1029/2003ja010243

Cosgrove, R. B., Tsunoda, R. T., Fukao, S., & Yamamoto, M. (2004). Coupling of the Perkins instability and the sporadic E layer instability derived from physical arguments. *Journal of Geophysical Research*, *109*(A6). https://doi.org/10.1029/2003ja010295

Crowley, G., Azeem, I., Reynolds, A., Duly, T. M., McBride, P., Winkler, C., & Hunton, D. (2016). Analysis of traveling ionospheric disturbances (TIDS) in GPS TEC launched by the 2011 Tohoku earthquake. *Radio Science*, *51*(5), 507–514. https://doi.org/10.1002/2015rs005907

Dong, W., Fritts, D. C., Lund, T. S., Wieland, S. A., & Zhang, S. (2020). Self-acceleration and instability of gravity wave packets: 2. Two-dimensional packet propagation, instability dynamics, and transient flow responses. *Journal of Geophysical Research*, *125*(3), e2019JD030691. https://doi.org/10.1029/2019jd030691

Drob, D. P., Emmert, J. T., Crowley, G., Picone, J. M., Shepherd, G. G., Skinner, W., et al. (2008). An empirical model of the earth's horizontal wind fields: HWM07. *Journal of Geophysical Research*, *113*(A12304). https://doi.org/10.1029/2008JA013668

Figueiredo, C. A. O. B., Takahashi, H., Wrasse, C. M., Otsuka, Y., Shiokawa, K., & Barros, D. (2018). Medium-scale traveling ionospheric disturbances observed by detrended total electron content maps over Brazil. *Journal of Geophysical Research: Space Physics*, *123*(3), 2215–2227. https://doi.org/10.1002/2017ja025021

Forbes, J. M., Bruinsma, S. L., Doornbos, E., & Zhang, X. (2016). Gravity wave-induced variability of the middle thermosphere. *Journal of Geophysical Research: Space Physics*, *121*(7), 6914–6923. https://doi.org/10.1002/2016ja022923

Franke, P., & Robinson, W. (1999). Nonlinear behavior in the propagation of atmospheric gravity waves. *Journal of the Atmospheric Sciences*, *56*, 3010–3027. https://doi.org/10.1175/1520-0469(1999)056<3010:nbitpo>2.0.co;2

Fritts, D. C., & Alexander, M. J. (2003). Gravity wave dynamics and effects in the middle atmosphere. *Reviews of Geophysics*, *41*(1). https://doi.org/10.1029/2001rg000106

Fritts, D. C., Dong, W., Lund, T. S., Wieland, S., & Laughman, B. (2020). Self-acceleration and instability of gravity wave packets: 3. Three-dimensional packet propagation, secondary gravity waves, momentum transport, and transient mean forcing in tidal winds. *Journal of Geophysical Research: Atmospheres*, *125*(3), e2019JD030692. https://doi.org/10.1029/2019jd030692

Fritts, D. C., Laughman, B., Lund, T. S., & Snively, J. B. (2015). Self-acceleration and instability of gravity wave packets: 1. Effects of temporal localization. *Journal of Geophysical Research: Atmosphere*, *120*, 8783–8803, 120. https://doi.org/10.1002/2015JD023363

Fritts, D. C., & Yuan, L. (1989). An analysis of gravity wave ducting in the atmosphere: Eckart's resonances in thermal and Doppler ducts. *Journal of Geophysical Research*, *94*(D15), 18455–18466. https://doi.org/10.1029/jd094id15p18455

Garcia, F. J., Kelley, M. C., Makela, J. J., & Huang, C.-S. (2000). Airglow observations of mesoscale low-velocity traveling ionospheric disturbances at midlatitudes. *Journal of Geophysical Research: Space Physics*, *105*(A8), 18407–18415. https://doi.org/10.1029/1999ja000305

Garcia, R. F., Bruinsma, S., Massarweh, L., & Doornbos, E. (2016). Medium-scale gravity wave activity in the thermosphere inferred from GOCE data. *Journal of Geophysical Research: Space Physics*, *121*(8), 8089–8102. https://doi.org/10.1002/2016ja022797

Gavrilov, N. M., & Kshevetskii, S. P. (2018). Features of the supersonic gravity wave penetration from the earth's surface to the upper atmosphere. *Radiophysics and Quantum Electronics*, *61*(4), 243–252. https://doi.org/10.1007/s11141-018-9885-4

Heale, C. J., Bossert, K., Vadas, S. L., Hoffmann, L., Dörnbrack, A., Stober, G., et al. (2020). Secondary gravity waves generated by breaking mountain waves over Europe. *Journal of Geophysical Research: Atmospheres*, *125*(5), e2019JD031662. https://doi.org/10.1029/2019jd031662

Heale, C. J., Lund, T. S., & Fritts, D. C. (2020). Convectively generated gravity waves during solstice and equinox conditions. *Journal of Geophysical Research: Atmospheres*, *125*(9), e2019JD031582. https://doi.org/10.1029/2019jd031582

Heale, C. J., Snively, J. B., Bhatt, A. N., Hoffmann, L., Stephan, C. C., & Kendall, E. A. (2019). Multilayer observations and modeling of thunderstorm-generated gravity waves over the midwestern United States. *Geophysical Research Letters*, *46*(23), 14164–14174. https://doi.org/10.1029/2019gl085934

Heale, C. J., Snively, J. B., Hickey, M. P., & Ali, C. J. (2014). Thermospheric dissipation of upward propagating gravity wave packets. *Journal of Geophysical Research*, *119*, 3857–3872. https://doi.org/10.1002/2013JA019387

Hernández-Pajares, M., Juan, J. M., Sanz, J., & Aragón-Àngel, A. (2012). Propagation of medium scale traveling ionospheric disturbances at different latitudes and solar cycle conditions. *Radio Science*, *47*(06). https://doi.org/10.1029/2011RS004951

Hickey, M. P., Schubert, G., & Walterscheid, R. L. (2009). Propagation of tsunami-driven gravity waves into the thermosphere and ionosphere. *Journal of Geophysical Research*, *114*(A8). https://doi.org/10.1029/2009ja014105

Hines, C. (1960). Internal atmospheric gravity waves at ionospheric heights. *Canadian Journal of Physics*, *38*. https://doi.org/10.1139/p60-150

Hocke, K., & Schlegel, K. (1996). A review of atmospheric gravity waves and travelling ionospheric disturbances: 1982–1995. *Annales Geophysicae*, *14*(9), 917–940. https://doi.org/10.1007/s00585-996-0917-6

Holton, J. R. (1983). The influence of gravity wave breaking on the general circulation of the middle atmosphere. *Journal of the Atmospheric Sciences*, *40*, 2497–2507. https://doi.org/10.1175/1520-0469(1983)040<2497:tiogwb>2.0.co;2

Holton, J. R., & Alexander, M. J. (2000). The role of waves in the transport circulation of the middle atmosphere. In G. M. Ser (Ed.), *Atmospheric science across the stratopause* (pp. 21–35). https://doi.org/10.1029/gm123p0021

Hooke, W. (1968). Ionospheric irregularities produced by internal atmospheric gravity waves. *Journal of Atmospheric and Terrestrial Physics*, *30*(5), 795–823. https://doi.org/10.1016/s0021-9169(68)80033-9

Horinouchi, T., Nakamura, T., & Kosaka, J.-i. (2002). Convectively generated mesoscale gravity waves simulated throughout the middle atmosphere. *Geophysical Research Letters*, *29*(21), 3–1. https://doi.org/10.1029/2002gl016069

Huang, F., Dou, X., Lei, J., Lin, J., Ding, F., & Zhong, J. (2016). Statistical analysis of nighttime medium-scale traveling ionospheric disturbances using airglow images and GPS observations over central China. *Journal of Geophysical Research: Space Physics*, *121*(9), 8887–8899. https://doi.org/10.1002/2016ja022760

Hunsucker, R. D. (1982). Atmospheric gravity waves generated in the high-latitude ionosphere: A review. *Reviews of Geophysics*, *20*(2), 293–315. https://doi.org/10.1029/rg020i002p00293

Inchin, P. A., Heale, C. J., Snively, J. B., & Zettergren, M. D. (2020). The dynamics of nonlinear atmospheric acoustic-gravity waves generated by tsunamis over realistic bathymetry. *Journal of Geophysical Research: Space Physics*, *125*(12), e2020JA028309. https://doi.org/10.1029/2020ja028309

Jones, W. (1970). A theory for quasi-periodic oscillations observed in the ionosphere. *Journal of Atmospheric and Terrestrial Physics*, *32*(9), 1555–1566. https://doi.org/10.1016/0021-9169(70)90071-1

Kelley, M., & Miller, C. (1997). Electrodynamics of midlatitude spread f 3. Electrohydrodynamic waves? A new look at the role of electric fields in thermospheric wave dynamics. *Journal of Geophysical Research*, *102*, 11539–11547. https://doi.org/10.1029/96JA03841

Kelley, M. C. (2011). On the origin of mesoscale TIDS at midlatitudes. *Annales Geophysicae*, *29*(2), 361–366. https://doi.org/10.5194/angeo-29-361-2011

Kelley, M. C., & Fukao, S. (1991). Turbulent upwelling of the mid-latitude ionosphere: 2. Theoretical framework. *Journal of Geophysical Research*, *96*(A3), 3747–3753. https://doi.org/10.1029/90ja02252

Kelley, M. C., & Makela, J. J. (2001). Resolution of the discrepancy between experiment and theory of midlatitude f-region structures. *Geophysical Research Letters*, *28*(13), 2589–2592. https://doi.org/10.1029/2000gl012777

Kirchengast, G. (1996). Elucidation of the physics of the gravity wave-TID relationship with the aid of theoretical simulations. *Journal of Geophysical Research*, *101*(A6), 13353–13368. https://doi.org/10.1029/96ja00750

Klostermeyer, J. (1972). Influence of viscosity, thermal conduction, and ion drag on the propagation of atmospheric gravity waves in the thermosphere. *Z GOEPHYS; DTSCH*, *38*(5), 881–890.

Kotake, N., Otsuka, Y., Ogawa, T., Tsugawa, T., & Saito, A. (2007). Statistical study of medium-scale traveling ionospheric disturbances observed with the GPS networks in southern California. *Earth Planets and Space*, *59*(2), 95–102. https://doi.org/10.1186/BF03352681

Kotake, N., Otsuka, Y., Tsugawa, T., Ogawa, T., & Saito, A. (2006). Climatological study of GPS total electron content variations caused by medium-scale traveling ionospheric disturbances. *Journal of Geophysical Research*, *111*(A4). https://doi.org/10.1029/2005ja011418

Krall, J., Huba, J. D., & Fritts, D. C. (2013). On the seeding of equatorial spread f by gravity waves. *Geophysical Research Letters*, *40*(4), 661–664. https://doi.org/10.1002/grl.50144

LeVeque, R. J. (2002). *Finite volume methods for Hyperbolic Problems (No. ISBN-0-521-00924-3)*. Cambridge Univ. Press.

LeVeque, R. J., & Berger, M. J. (2004). *Clawpack software version 4.6*. Retrieved from www.clawpack.org

Lindzen, R. S. (1981). Turbulence and stress owing gravity wave and tidal breakdown. *Journal of Geophysical Research*, *86*(C10), 9707–9714. https://doi.org/10.1029/jc086ic10p09707

Lund, T. S., & Fritts, D. C. (2012). Numerical simulation of gravity wave breaking in the lower thermosphere. *Journal of Geophysical Research*, *117*(D21105). https://doi.org/10.1029/2012JD017536

MacDougall, J., Abdu, M. A., Batista, I., Buriti, R., Medeiros, A. F., Jayachandran, P. T., & Borba, G. (2011). Spaced transmitter measurements of medium scale traveling ionospheric disturbances near the equator. *Geophysical Research Letters*, *38*(16). https://doi.org/10.1029/2011gl048598

Makela, J. J., Miller, E. S., & Talaat, E. R. (2010). Nighttime medium-scale traveling ionospheric disturbances at low geomagnetic latitudes. *Geophysical Research Letters*, *37*(24). https://doi.org/10.1029/2010gl045922

Martinis, C., Baumgardner, J., Wroten, J., & Mendillo, M. (2010). Seasonal dependence of MSTIDS obtained from 630.0 nm airglow imaging at Arecibo. *Geophysical Research Letters*, *37*(11). https://doi.org/10.1029/2010gl043569

McFarlane, N. A. (1987). The effect of orographically excited gravity wave drag on the general circulation of the lower stratosphere and troposphere. *Journal of the Atmospheric Sciences*, *44*, 1775–1800. https://doi.org/10.1175/1520-0469(1987)044<1775:teooeg>2.0.co;2

Miyoshi, Y., Jin, H., Fujiwara, H., & Shinagawa, H. (2018). Numerical study of traveling ionospheric disturbances generated by an upward propagating gravity wave. *Journal of Geophysical Research: Space Physics*, *123*(3), 2141–2155. https://doi.org/10.1002/2017ja025110

Munro, G. H. (1948). Short-period changes in the f region of the ionosphere. *Nature*, *162*(4127), 886–887. https://doi.org/10.1038/162886a0

Narayanan, V. L., Shiokawa, K., Otsuka, Y., & Neudegg, D. (2018). On the role of thermospheric winds and sporadic e layers in the formation and evolution of electrified MSTIDS in geomagnetic conjugate regions. *Journal of Geophysical Research: Space Physics*, *123*(8), 6957–6980. https://doi.org/10.1029/2018ja025261

Nicolls, M. J., Vadas, S. L., Aponte, N., & Sulzer, M. P. (2014). Horizontal parameters of daytime thermospheric gravity waves and E region neutral winds over Puerto Rico. *Journal of Geophysical Research: Space Physics*, *119*(1), 575–600. https://doi.org/10.1002/2013ja018988

Nishioka, M., Tsugawa, T., Kubota, M., & Ishii, M. (2013). Concentric waves and short-period oscillations observed in the ionosphere after the 2013 MOORE EF5 Tornado. *Geophysical Research Letters*, *40*(21), 5581–5586. https://doi.org/10.1002/2013gl057963

Oinats, A. V., Nishitani, N., Ponomarenko, P., Berngardt, O. I., & Ratovsky, K. G. (2016). Statistical characteristics of medium-scale traveling ionospheric disturbances revealed from the Hokkaido east and Ekaterinburg HF radar data. *Earth Planets and Space*, *68*(1), 8. https://doi.org/10.1186/s40623-016-0390-8

Otsuka, Y. (2018). Review of the generation mechanisms of post-midnight irregularities in the equatorial and low-latitude ionosphere. *Progress in Earth and Planetary Science*, *5*(1), 57. https://doi.org/10.1186/s40645-018-0212-7

Otsuka, Y., Kotake, N., Shiokawa, K., Ogawa, T., Tsugawa, T., & Saito, A. (2011). Statistical study of medium-scale traveling ionospheric disturbances observed with a GPS receiver network in Japan. In M. A. Abdu, & D. Pancheva (Eds.), *Aeronomy of the earth's atmosphere and ionosphere* (pp. 291–299). Springer Netherlands. https://doi.org/10.1007/978-94-007-0326-1_21

Otsuka, Y., Suzuki, K., Nakagawa, S., Nishioka, M., Shiokawa, K., & Tsugawa, T. (2013). GPS observations of medium-scale traveling ionospheric disturbances over Europe. *Annales Geophysicae*, *31*(2), 163–172. https://doi.org/10.5194/angeo-31-163-2013

Park, J., Lühr, H., Kervalishvili, G., Rauberg, J., Michaelis, I., Stolle, C., & Kwak, Y.-S. (2015). Nighttime magnetic field fluctuations in the topside ionosphere at midlatitudes and their relation to medium-scale traveling ionospheric disturbances: The spatial structure and scale sizes. *Journal of Geophysical Research: Space Physics*, *120*(8), 6818–6830. https://doi.org/10.1002/2015ja021315

Paulino, I., Medeiros, A. F., Vadas, S. L., Wrasse, C. M., Takahashi, H., Buriti, R. A., et al. (2016). Periodic waves in the lower thermosphere observed by oi 630nm airglow images. *Annales Geophysicae*, *34*(2), 293–301. https://doi.org/10.5194/angeo-34-293-2016

Perkins, F. (1973). Spread f and ionospheric currents. *Journal of Geophysical Research (1896–1977)*, *78*(1), 218–226. https://doi.org/10.1029/ja078i001p00218

Picone, J. M., Hedin, A. E., Drob, D. P., & Aikin, A. (2002). NRL-MSISE-00 empirical model of the atmosphere: Statistical comparisons and scientific issues. *Journal of Geophysical Research*, *107*(A12), 1–21. https://doi.org/10.1029/2002ja009430

Pimenta, A. A., Amorim, D. C. M., & Candido, C. M. N. (2008). Thermospheric dark band structures at low latitudes in the southern hemisphere under different solar activity conditions: A study using oi 630 nm emission all-sky images. *Geophysical Research Letters*, *35*(16). https://doi.org/10.1029/2008gl034904

Pitteway, M. L. V., & Hines, C. O. (1963). The viscous damping of atmospheric gravity waves. *Canadian Journal of Physics*, *41*, 1935–1948. https://doi.org/10.1139/p63-194

Rajesh, P. K., Liu, J. Y., Lin, C. H., Chen, A. B., Hsu, R. R., Chen, C. H., & Huba, J. D. (2016). Space-based imaging of nighttime medium-scale traveling ionospheric disturbances using FORMOSAT-2/ISUAL 630.0 nm airglow observations. *Journal of Geophysical Research: Space Physics*, *121*(5), 4769–4781. https://doi.org/10.1002/2015ja022334

Röttger, J. (1977). Travelling disturbances in the equatorial ionosphere and their association with penetrative cumulus convection. *Journal of Atmospheric and Terrestrial Physics*, *39*(9), 987–998.

Saito, A., Fukao, S., & Miyazaki, S. (1998). High resolution mapping of tec perturbations with the GSI GPS network over Japan. *Geophysical Research Letters*, *25*(16), 3079–3082. https://doi.org/10.1029/98gl52361

Scinocca, J. F., & Ford, R. (2000). The nonlinear forcing of large-scale internal gravity waves by stratified shear instability. *Journal of the Atmospheric Sciences*, *57*(5), 653–672. https://doi.org/10.1175/1520-0469(2000)057<0653:tnfols>2.0.co;2

Shiokawa, K., Ihara, C., Otsuka, Y., & Ogawa, T. (2003). Statistical study of nighttime medium-scale traveling ionospheric disturbances using midlatitude airglow images. *Journal of Geophysical Research*, *108*(A1). https://doi.org/10.1029/2002ja009491

Snively, J., & Pasko, V. P. (2003). Breaking of thunderstorm-generated gravity waves as a source of short-period ducted waves at mesopause altitudes. *Geophysical Research Letters*, *30*(24). https://doi.org/10.1029/2003gl018436

Snively, J. B. (2013). Mesospheric hydroxyl airglow signatures of acoustic and gravity waves generated by transient tropospheric forcing. *Geophysical Research Letters*, *40*, 4533–4537. https://doi.org/10.1002/grl.50886

Snively, J. B. (2017). Nonlinear gravity wave forcing as a source of acoustic waves in the mesosphere, thermosphere, and ionosphere. *Geophysical Research Letters*, *44*(23), 12020–12. https://doi.org/10.1002/2017gl075360

Snively, J. B., & Pasko, V. P. (2008). Excitation of ducted gravity waves in the lower thermosphere by tropospheric sources. *Journal of Geophysical Research*, *113*. https://doi.org/10.1029/2007ja012693

Stull, R. (2017). *Practical meteorology: An algebra-based survey of atmospheric science*. Univ. of British Columbia.

Sutherland, B. R., & Yewchuk, K. (2004). Internal wave tunneling. *Journal of Fluid Mechanics*, *511*, 125–134. https://doi.org/10.1017/s0022112004009863

Takahashi, H., Wrasse, C. M., Figueiredo, C. A. O. B., Barros, D., Paulino, I., Essien, P., et al. (2020). Equatorial plasma bubble occurrence under propagation of MSTID and MLT gravity waves. *Journal of Geophysical Research: Space Physics*, *125*(9), e2019JA027566. https://doi.org/10.1029/2019JA027566

Torrence, C., & Compo, G. P. (1998). A practical guide to wavelet analysis. *Bulletin of the American Meteorological Society*, *79*(1), 61–78. https://doi.org/10.1175/1520-0477(1998)079<0061:apgtwa>2.0.co;2

Tsugawa, T., Otsuka, Y., Coster, A. J., & Saito, A. (2007). Medium-scale traveling ionospheric disturbances detected with dense and wide TEC maps over North America. *Geophysical Research Letters*, *34*(22). https://doi.org/10.1029/2007GL031663

Tsunoda, R. T. (2010). On equatorial spread f: Establishing a seeding hypothesis. *Journal of Geophysical Research*, *115*(A12). https://doi.org/10.1029/2010JA015564

Vadas, S. L. (2007). Horizontal and vertical propagation and dissipation of gravity waves in the thermosphere from lower atmospheric and thermospheric sources. *Journal of Geophysical Research*, *112*(0630). https://doi.org/10.1029/2006ja011845

Vadas, S. L., & Azeem, I. (2021). Concentric secondary gravity waves in the thermosphere and ionosphere over the continental United States on 25-26 march 2015 from deep convection. *Journal of Geophysical Research: Space Physics*, *126*, e2020JA028275. https://doi.org/10.1029/2020JA028275

Vadas, S. L., & Becker, E. (2019). Numerical modeling of the generation of tertiary gravity waves in the mesosphere and thermosphere during strong mountain wave events over the southern Andes. *Journal of Geophysical Research: Space Physics*, *124*(9), 7687–7718. https://doi.org/10.1029/2019JA026694

Vadas, S. L., & Crowley, G. (2010). Sources of the traveling ionospheric disturbances observed by the ionospheric TIDDBIT sounder near wallops island on 30 October 2007. *Journal of Geophysical Research*, *115*(A7). https://doi.org/10.1029/2009JA015053

Vadas, S. L., & Crowley, G. (2017). Neutral wind and density perturbations in the thermosphere created by gravity waves observed by the TIDDBIT sounder. *Journal of Geophysical Research: Space Physics*, *122*(6), 6652–6678. https://doi.org/10.1002/2016JA023828

Vadas, S. L., & Fritts, D. C. (2005). Thermospheric responses to gravity waves: Influences of increasing viscosity and thermal diffusivity. *Journal of Geophysical Research*, *110*, D15103. https://doi.org/10.1029/2004jd005574

Vadas, S. L., Fritts, D. C., & Alexander, M. J. (2003). Mechanism for the generation of secondary waves in wave breaking regions. *Journal of the Atmospheric Sciences*, *60*, 194–214. https://doi.org/10.1175/1520-0469(2003)060<0194:mftgos>2.0.co;2

Vadas, S. L., & Liu, H. L. (2009). Generation of large scale gravity waves and neutral winds in the thermosphere from the dissipation of convectively generated gravity waves. *Journal of Geophysical Research*, *114*. https://doi.org/10.1029/2009ja014108

Vadas, S. L., Xu, S., Yue, J., Bossert, K., Becker, E., & Baumgarten, G. (2019). Characteristics of the quiet-time hot spot gravity waves observed by GOCE over the southern Andes on 5 July 2010. *Journal of Geophysical Research: Space Physics*, *124*. https://doi.org/10.1029/2019JA026693

Vadas, S. L., Yue, J., She, C.-Y., Stamus, P. A., & Liu, A. Z. (2009). A model study of the effects of winds on concentric rings of gravity waves from a convective plume near Fort Collins on 11 May 2004. *Journal of Geophysical Research*, *114*(D6). https://doi.org/10.1029/2008JD010753

Vadas, S. L., Zhao, J., Chu, X., & Becker, E. (2018). The excitation of secondary gravity waves from body forces: Theory and observation. *Journal of Geophysical Research: Atmosphere*, *123*. https://doi.org/10.1029/2017JD027970

Vincent, R. A., Alexander, M. J., Dolman, B. K., MacKinnon, A. D., May, P. T., Kovalam, S., & Reid, I. M. (2013). Gravity wave generation by convection and momentum deposition in the mesosphere? Lower thermosphere. *Journal of Geophysical Research*, *118*(12), 6233–6245. https://doi.org/10.1002/jgrd.50372

Waldock, J., & Jones, T. (1986). Hf Doppler observations of medium-scale travelling ionospheric disturbances at mid-latitudes. *Journal of Atmospheric and Terrestrial Physics*, *48*(3), 245–260. https://doi.org/10.1016/0021-9169(86)90099-1

Walterscheid, R., Schubert, G., & Brinkman, D. (2001). Small-scale gravity waves in the upper mesosphere and lower thermosphere generated by deep tropical convection. *Journal of Geophysical Research*, *106*(D23), 31825–31832. https://doi.org/10.1029/2000jd000131

Walterscheid, R. L., & Hecht, J. H. (2003). A reexamination of evanescent acoustic-gravity waves: Special properties and aeronomical significance. *Journal of Geophysical Research*, *108*(D11). https://doi.org/10.1029/2002JD002421

Xiao, Z., Xiao, S.-g., Hao, Y.-q., & Zhang, D.-h. (2007). Morphological features of ionospheric response to typhoon. *Journal of Geophysical Research*, *112*(A4). https://doi.org/10.1029/2006JA011671

Xu, S., Yue, J., Xue, X., Vadas, S. L., Miller, S. D., Azeem, I., et al. (2019). Dynamical coupling between hurricane Matthew and the middle to upper atmosphere via gravity waves. *Journal of Geophysical Research: Space Physics*, *124*(5), 3589–3608. https://doi.org/10.1029/2018JA026453

Yeh, K. C., & Liu, C. H. (1974). Acoustic-gravity waves in the upper atmosphere. *Reviews of Geophysics*, *12*(2), 193–216. https://doi.org/10.1029/RG012i002p00193

Yokoyama, T., Hysell, D. L., Otsuka, Y., & Yamamoto, M. (2009). Three-dimensional simulation of the coupled Perkins and Es-layer instabilities in the nighttime midlatitude ionosphere. *Journal of Geophysical Research: Space Physics*, *114*(A3). https://doi.org/10.1029/2008JA013789

Zettergren, M. D., & Snively, J. B. (2015). Ionospheric response to infrasonic-acoustic waves generated by natural hazard events. *Journal of Geophysical Research: Space Physics*, *120*(9), 8002–8024. https://doi.org/10.1002/2015JA021116

Zhou, X., Holton, J. R., & Mullendore, G. L. (2002). Forcing of secondary waves by breaking of gravity waves in the mesosphere. *Journal of Geophysical Research*, *107*(D7), 1–7. https://doi.org/10.1029/2001JD001204

Stephan, C., & Alexander, M. J. (2015). Realistic simulations of atmospheric gravity waves over the continental U.S. using precipitation radar data. *Journal of Advances in Modeling Earth Systems*, *7*(2), 823–835. https://doi.org/10.1002/2014MS000396